From Exploration to Structured Navigation: Learning Dynamics of Freely Moving Marmosets during Foraging

Nada El Mahmoudi[1]*†, Francesca Lanzarini[1]†, Farzad Ziaie Nezhad[1], Deepak Surendran[1], Jean Laurens[1]*

1- Ernst Strüngmann Institute (ESI) for Neuroscience in Cooperation with Max Planck Society, Frankfurt am Main, 60528, Germany

† These authors contributed equally to this work

*Corresponding authors: jean.laurens@esi-frankfurt.de; nada.el-mahmoudi@univ-amu.fr

Abstract

Spatial memory plays a crucial role in guiding navigation and optimizing foraging efficiency. While extensive research has explored navigation strategies in rodents, how these strategies emerge and evolve in freely moving non-human primates remains poorly understood. Here, we conducted a longitudinal study to investigate the dynamics of spatial learning and navigation strategies in freely moving common marmosets (*Callithrix jacchus)* performing a foraging task in a semi-naturalistic environment. Marmosets were trained to collect rewards from eight spatially distributed dispensers. Using behavioral analyses combined with machine learning methods, including unsupervised clustering and probabilistic modeling, we examined how their navigation strategies evolved over time. Our results reveal a progressive improvement in performance, accompanied by an increasing structuring of movement patterns. Initially, marmosets exhibited exploratory behaviors, with high transition variability between food dispensers. As training progressed, their navigation became more structured, with the emergence of recurrent transition patterns and a shift towards route-based navigation. However, despite this increasing regularity, their navigation retained a degree of flexibility, allowing them to dynamically adapt their routes rather than following a fixed sequence. These findings suggest that marmosets develop structured yet flexible navigation strategies through experience. Their behavior reflects a balance between efficiency and adaptability and supports the emergence of a flexible representation of space. Our study provides novel insights into spatial memory development in primates and highlights the value of semi-naturalistic paradigms for studying navigation strategies and spatial learning in freely moving animals.

Keywords

Common marmosets; Neuroethology; Spatial memory; Navigation strategies; Foraging behavior;

Introduction

Spatial memory is a fundamental cognitive function that allows an animal to track its own location in space by remembering where it has been[1]. Traditionally, a distinction is made between spatial working memory, which allows the retention of information over short periods, and spatial reference memory, which supports long-term information retention [2]. Both forms of memory are essential for navigation, as they provide the foundation for different navigation strategies by allowing individuals to recall, organize, and use spatial information efficiently based on available cues and past experiences.

All navigation strategies rely on spatial memory, yet they differ in how they process and utilize stored information to guide movement and decision-making [3–6]. Route-based navigation relies on recalling and following fixed sequences of learned subgoals along habitual paths, demonstrating a structured use of spatial memory to retrace familiar routes. In contrast, topological navigation constructs a network of interconnected locations, allowing for more flexible path selection, while still relying on memory to recognize spatial relationships. Finally, metric navigation encodes precise distances and directions between locations, enabling shortcut-taking and novel route computation by integrating spatial memory with geometric processing [7,8].

While navigation strategies have been extensively studied in rodents [9–13] non-human primates (NHPs) also exhibit complex spatial behaviors, integrating memory and environmental cues to optimize foraging efficiency[14]. However, how spatial memory and navigation strategies emerge and evolve remains poorly understood, particularly in freely moving NHPs [14,15].

Among NHPs, common marmosets (*Callithrix jacchus*) provide a valuable model for studying spatial navigation, as they are small arboreal primates that rely on complex movement patterns to forage and navigate their environment [16–19]. Since their diet includes seasonally available resources such as fruits and insects, alongside more stable food sources like tree exudates, marmosets must rely on both short-term and long-term spatial memory to track changing resource locations and adjust their foraging strategies accordingly.

Field studies have shown that wild common marmosets can retain spatial information over both short and long timescales and even remember the location of food sources after a single visit, an ability that enhances foraging efficiency in environments where resource availability fluctuates [20].

Recent findings suggest that wild common marmosets predominantly employ a route-based navigation strategy, systematically reusing specific travel paths and relying on habitual routes to reach feeding and resting sites [21]. However, their navigation is not strictly sequential; instead, their routes appear to follow a topological, network-like structure, with interconnected paths that allow them to adapt to environmental constraints while still relying on familiar routes [21].

While these findings shed light on wild marmoset navigation, little is known about how spatial memory and navigation strategies develop in controlled environments, despite the growing recognition of common marmosets as a promising model for spatial cognition [22,23]. Research by MacDonald et al. (1994) showed that captive marmosets can remember the locations of food sources and avoid revisiting previously depleted sites, demonstrating well-developed spatial working memory [24]. In addition, it was found that marmosets can use landmarks to guide their searches for goals, highlighting their ability to rely on external cues for navigation [25]. However, these studies did not investigate the dynamics of spatial learning or how navigation strategies emerge and evolve over time. Furthermore, they were conducted in relatively simple environments, lacking the complexity of more ecologically relevant settings where sophisticated navigation strategies might emerge.

In this study, we investigated how freely moving marmosets develop and refine their navigation strategies in a spatial working memory task within an enriched, semi-naturalistic environment. Our findings reveal a spontaneous and continuous improvement in performance, characterized by the progressive structuring of movement patterns and the emergence of consistent navigation choices over time. While marmosets increasingly relied on structured routes, they retained a degree of flexibility, allowing them to dynamically adapt their foraging strategies. This interplay between habitual pathways and adaptive decision-making highlights the sophistication of their spatial navigation. By bridging the gap between controlled experimental paradigms and ecologically relevant navigation, our study provides new insights into how primates dynamically optimize foraging efficiency through spatial learning.

Results

To examine the dynamics of spatial learning and the evolution of navigation behavior in common marmosets, we implemented a spatial working memory task in an enriched, semi-naturalistic environment (**Fig. 1A**). Marmosets navigated freely within the setup, collecting rewards from eight food dispensers (**Fig. 1E**) distributed around the apparatus. Each trial began with the activation of the dispenser at the center of the setup (i.e., the "Home Dispenser"). This activation was signaled by acoustic and visual cues, along with reward delivery. The subject had to move towards the Home Dispenser, after which all eight dispensers were simultaneously activated, delivering reward (**Fig. 1B**). To complete the trial, the monkey had to visit all eight dispensers at least once, collecting the reward from each. The trial ended upon the first visit to the eighth unique dispenser, regardless of any revisits along the way. However, if the monkey did not visit all eight dispensers within 10 minutes, the trial was automatically terminated. After trial completion or timeout, the Home Dispenser was reactivated, signaling the start of the next trial. The marmosets explored the environment and collected rewards, which allowed us to investigate spatial working memory and navigation strategies in the context of spontaneous foraging. Each monkey underwent 30 training sessions, with an average of 7.96 ± 0.4 trials for Animal E and 8 ± 0.4 trials for Animal F per session.

Marmosets show stable dispenser interactions and distinct learning dynamics across error types

To assess marmoset interactions with the dispensers, we analyzed the total number of visits and omissions (i.e., dispensers not visited within a trial) for each dispenser (**Fig**. **1C-D**). A Chi-squared test revealed significant deviations from uniformity in the distribution of visits for both Animal E ($\chi^2 = 15.47$, df = 7, $p = 0.03$) and Animal F ($\chi^2 = 33.6$, df = 7, $p < 0.001$). However, post-hoc binomial tests with Bonferroni correction showed that Animal E visited all dispensers at similar frequencies ($p > 0.05$). Animal F visited Dispenser 1 significantly less often than expected ($p < 0.05$), while visit frequencies for the other dispensers remained uniform. For omissions, neither animal showed significant deviations from uniformity (Animal E: $\chi^2 = 8.9$, df = 7, $p = 0.26$; Animal F: $\chi^2 = 9.89$, df = 7, $p = 0.19$), indicating that dispensers were omitted at similar rates across trials. Overall, while a global deviation in visit distribution was observed,

only Dispenser 1 in Animal F showed a significant difference, whereas omissions followed a uniform distribution for both animals.

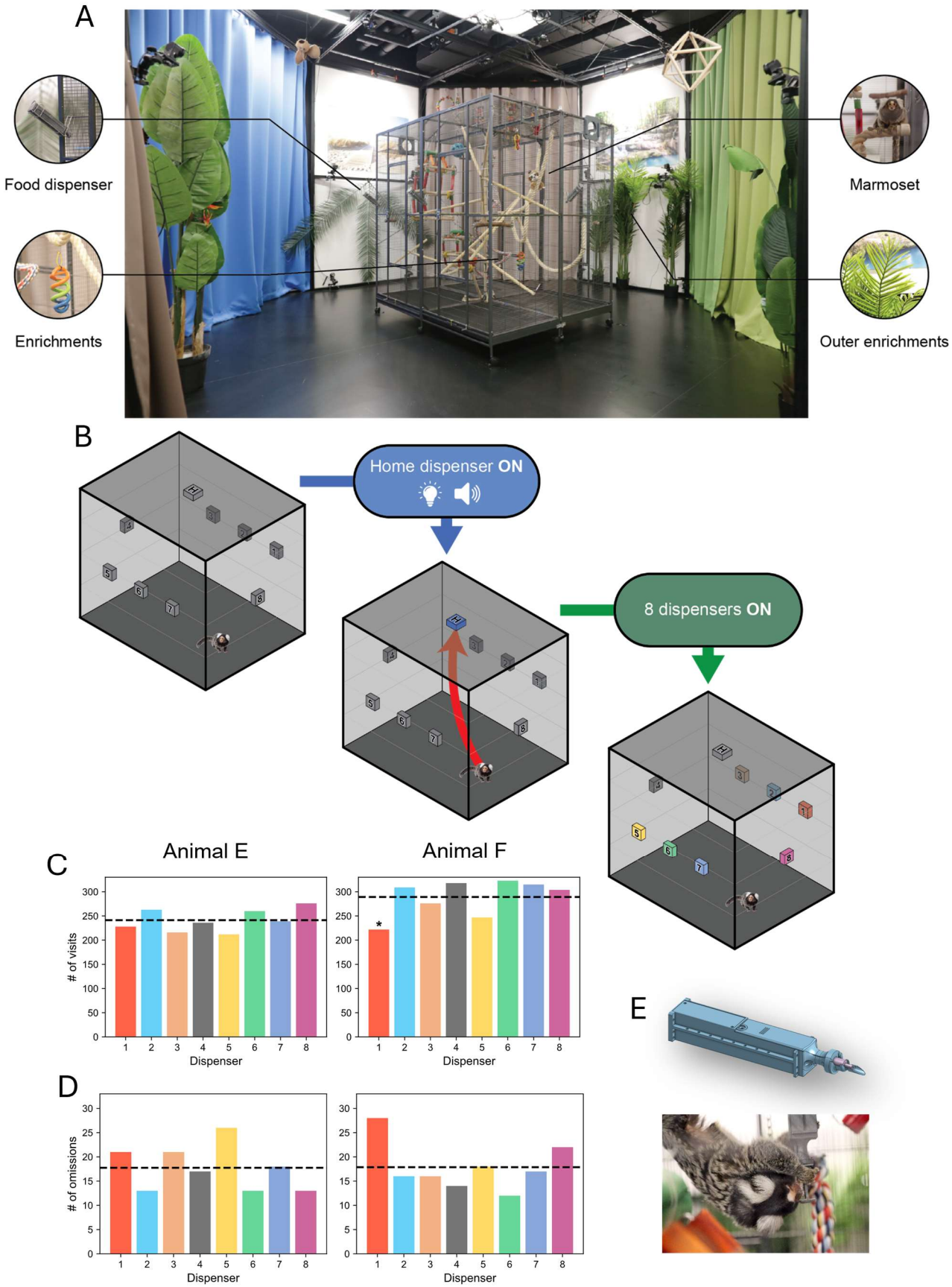

Figure 1: A Freely Moving Setup for Marmosets to Investigate Spatial Memory during Foraging
A. Experimental setup. The enclosure consisted of a wire mesh cage (1.8 m × 1.4 m × 1.6 m; 4 m³) that allowed the marmosets to climb and move freely. Inside, structural enrichments—such as wooden sticks, semi-rigid ropes, and various objects—encouraged locomotion and exploration. External cues were provided by four white walls, four colored curtains, and large plastic plants. An action camera was mounted above the setup to record behavioral data. A food dispenser, designated as the Home Dispenser (HD), was mounted centrally on the ceiling, and eight additional food dispensers were evenly distributed around the perimeter of the cage to deliver rewards during the task. **B. Trial design**. At the start of each trial, the Home Dispenser (HD) was activated with an LED and a buzzer. Once the marmoset reached the HD, all eight peripheral dispensers were remotely activated, delivering gum arabic. To complete the trial, the subject had to visit every dispenser at least once; otherwise, the trial was terminated after a 10-minute timeout. **C. Total visits per dispenser**. Bar plot showing the total number of visits to each of the eight dispensers for Animal E (left) and Animal F (right). The dashed horizontal line represents the expected number of visits under a uniform distribution. A chi-squared test was performed to assess the overall distribution, followed by a binomial test for each dispenser against the theoretical proportion. Significant p-values from the binomial test are marked with an asterisk (*$p < 0.05$), with p-values corrected for multiple comparisons using the Bonferroni method. **D. Total omissions per dispenser**. Bar plot showing the total number of omissions to each of the eight dispensers for Animal E (left) and Animal F (right). The dashed horizontal line represents the expected number of omissions under a uniform distribution. A chi-squared test was performed to assess the overall distribution. **E. Reward dispenser design**. Design of the custom-made food dispenser used during the experiment (top) Eight dispensers were placed around the setup, while the HD was placed at the center of the ceiling upside-down (bottom, a marmoset eating from the HD).

To evaluate the marmosets' task performance, we measured the mean number of errors for each training session and performed a linear regression to assess changes in performance over time (**Fig. S1**). Both animals exhibited a significant decrease in the mean number of errors across training sessions, indicating an improvement in performance over time (Animal E: $R^2 = 0.26$, $p < 0.01$, slope=-0.07; Animal F: $R^2 = 0.62$, $p < 0.001$, slope=-0.28).

We further explored potential influences on performance using a multiple linear regression model (**Table S1**). However, our results confirmed that performance improvements were primarily driven by the number of training sessions, with no detectable effect from other factors.

To gain deeper insights into marmoset performance, we categorized and analyzed the different types of errors observed during training sessions. We identified three types of errors: repetition errors (returning to a dispenser already visited during the trial), omission errors (failing to visit a dispenser during the trial), and rule errors (returning to the home dispenser during the trial).Our analysis revealed distinct error patterns at both the session and trial levels: while rule and repetition errors were more frequent in trials with higher visit counts, omission errors occurred independently from other error types and often appeared in isolation (**Fig. S1, Appendix 1**).

Clustering analysis reveals different task execution profiles

Building on the observed differences in error types and their relationships with task metrics, we performed an unsupervised clustering analysis to capture trial-level variability in task execution. Since rule and repetition errors correlate with the number of visits, we used two key metrics: omission errors and the total number of visits. The k-means algorithm identified four distinct clusters for each animal, representing unique profiles of task execution (**Fig. 2A**). The optimal number of clusters ($k = 4$) was determined using the silhouette score and the inertia, which evaluate the consistency and separation of clusters. Jitter was added to enhance visualization.

For Animal E, the silhouette score was 0.74, and the inertia was 39.5, indicating good separation between clusters. For Animal F, the silhouette score was 0.68, and the inertia was 56.43, reflecting moderate-to-good separation. These values indicate that the clustering accurately and similarly captured the variability in task execution across trials in both animals. The numerical values of the clusters' centroids (**Fig. 2A**) are reported in **Table S2** (mean ± SEM). To further characterize these clusters, we compared key performance parameters across them, including the total number of visits, errors, and trial duration (**Fig. S3**).

Cluster 0 was characterized by the lowest total number of errors and the shortest trial durations compared to all other clusters ($p < 0.001$ for both animals). These features indicate

that Cluster 0 reflects an optimal state of task performance, where the animals were fully engaged, adhered to task rules, and performed with high efficiency and precision.

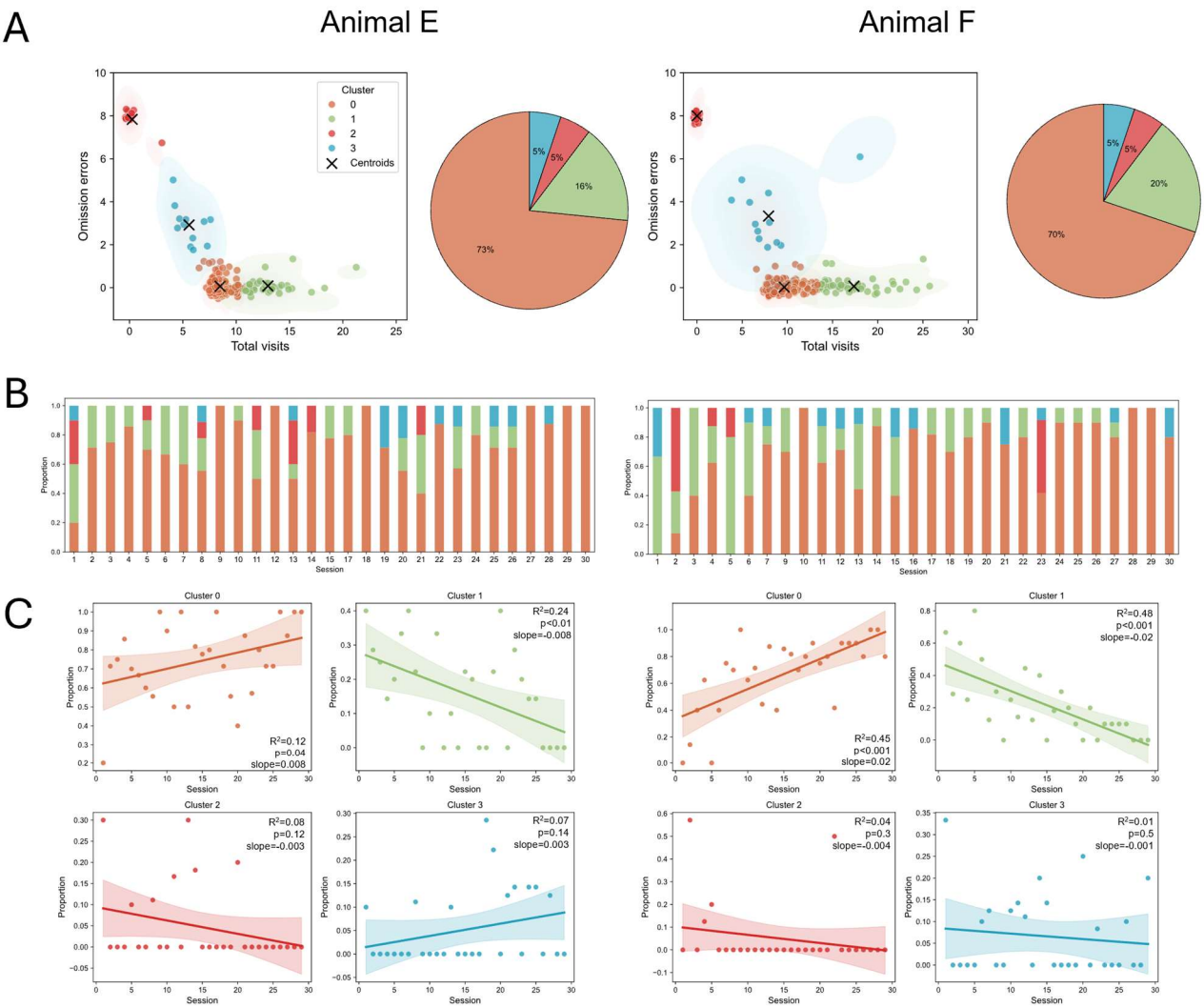

Figure 2: Clustering analysis reveals different task execution profiles A. Unsupervised clustering analysis Scatter plot showing the results of the K-means clustering analysis, with each trial assigned to one of four clusters, represented by different colors, for Animal E (left) and Animal F (right). The centroids of the clusters, defined by omission errors and total visits, are marked with crosses. Data points are jittered for enhanced visibility for each animal. A pie chart shows the relative proportion of trials assigned to each of the four clusters; colors follow the legend from Cluster analysis. **B. Proportions of cluster distributions across training sessions.** Stacked bar plot showing the normalized proportion of trials assigned to each cluster across training sessions for Animal E (left) and Animal F (right). The bars represent the relative frequency of trials in each cluster, with each segment of the bar corresponding to the proportion of trials within a specific cluster. The color of each segment corresponds to the assigned cluster, with Cluster 0 shown in orange, Cluster 1 in green, Cluster 2 in red, and Cluster 3 in blue. **C. Linear regression of cluster proportions across training sessions.** Scatter plots showing the proportion of trials assigned to each cluster across training sessions for Animal E (left) and Animal F (right). The regression lines represent the best-fit linear model for each cluster, with shaded areas indicating the 95% confidence intervals for the predictions. The color of each line and scatter plot corresponds to the cluster: Cluster 0 (orange), Cluster 1 (green), Cluster 2 (red), and Cluster 3 (blue).

In comparison, **Cluster 1** exhibited a significantly higher number of visits and increased rule, and repetition errors compared to all other clusters ($p < 0.001$ for both animals). Despite the elevated error counts, omission errors in this cluster were near zero. These characteristics indicate that Cluster 1 represents a state of active engagement where animals participated in the task but faced challenges in execution precision.

Cluster 2 displayed the highest omission errors and a complete lack of visits. These features indicate that Cluster 2 represents a state of disengagement, where the animals showed little to no interaction with the task.

Lastly, **Cluster 3** was characterized by significantly fewer visits and more omissions than Cluster 0 and Cluster 1. However, animals tended to make slightly more visits and fewer omissions than in Cluster 2, although these differences were not statistically significant. These features indicate that Cluster 3 represents a state of partial engagement, where the animals initiated task-related behaviors but failed to fully execute the task.

These results highlight distinct task execution strategies, revealing behavioral variability across clusters. To further explore these differences, we examined the proportion of trials assigned to each cluster and how these proportions evolved over time. The distributions of trials falling into each cluster were remarkably similar between the two animals, indicating comparable patterns in their behavioral performance (**Fig. 2A**). Clusters 0 and 1 accounted for most trials (89% for Animal E, 90% for Animal F), whereas Clusters 2 and 3 comprised only 10% of trials in both animals.

To explore how these cluster distributions evolved over time, we performed linear regression analyses to assess the temporal trends in cluster proportions (**Fig. 2B-C**). Over training, the distributions of Clusters 0 and 1 evolved in opposite directions: Cluster 0 significantly increased (Animal E: $R^2 = 0.12$, $p = 0.04$, slope = 0.008; Animal F: $R^2 = 0.45$, $p < 0.001$, slope = 0.02) reflecting a shift toward optimized task execution, whereas Cluster 1 significantly decreased (Animal E: $R^2 = 0.24$, $p < 0.01$, slope = -0.008; Animal F: $R^2 = 0.48$, $p < 0.001$, slope = -0.02) indicating a reduction in execution errors and imprecision. In contrast, the regressions were not significant ($p<0.05$) for Clusters 2 and 3, indicating that disengagement levels did not vary significantly across sessions.

Altogether, these findings indicate that Clusters 0 and 1 reflect task-related engagement, whereas Clusters 2 and 3 correspond to disengaged behavioral states unrelated to task execution.

Clusters 0 and 1 reflect variations in efficiency within a shared behavioral framework

Since Clusters 0 and 1 are associated with task engagement, we then asked whether these two clusters reflect fundamentally distinct task execution strategies or simply variations in task precision and efficiency. To address this question, we focused on the first eight choices within each trial, since a successful completion of the trial requires visiting eight dispensers without repetitions.

We quantified the performance rate as the average percentage of correct responses within the first eight choices of each trial (**Fig. 3A; H**), where a response was considered correct if the animal visited a dispenser that had not yet been visited during that trial. To determine whether performance deviated from random behavior, we compared performance rates to an expected chance level of 50%, assuming all dispensers (including the central one) had an equal probability of being visited. The Wilcoxon signed-rank test with Bonferroni correction revealed that both clusters exhibited significantly greater performance rates than chance ($p < 0.001$, for both animals), confirming that even in Cluster 1, where execution was less precise, marmosets exhibited goal-directed rather than random behavior.

To further explore how they navigated the environment, we analyzed their transitions between dispensers within a trial, i.e., how they moved from one dispenser to another. By reconstructing sequences of dispenser visits, we captured the ordered series of choices an animal made within a trial.

To analyze the overall organization of the transitions we used two global metrics: global entropy, which measures uncertainty in transition patterns, and global transition diversity,

which captures the evenness of transition probabilities. In our framework, high entropy reflects unpredictable, wide-ranging transitions, while low entropy indicates a reliance on a smaller set of recurrent transitions. Similarly, high diversity corresponds to evenly distributed transitions, whereas low diversity signifies a preference for specific paths.

For both animals, entropy and transition diversity were significantly lower than chance ($p < 0.001$, based on bootstrap-generated distributions of 1,000 random transitions; **Fig. 3B-C; I-**

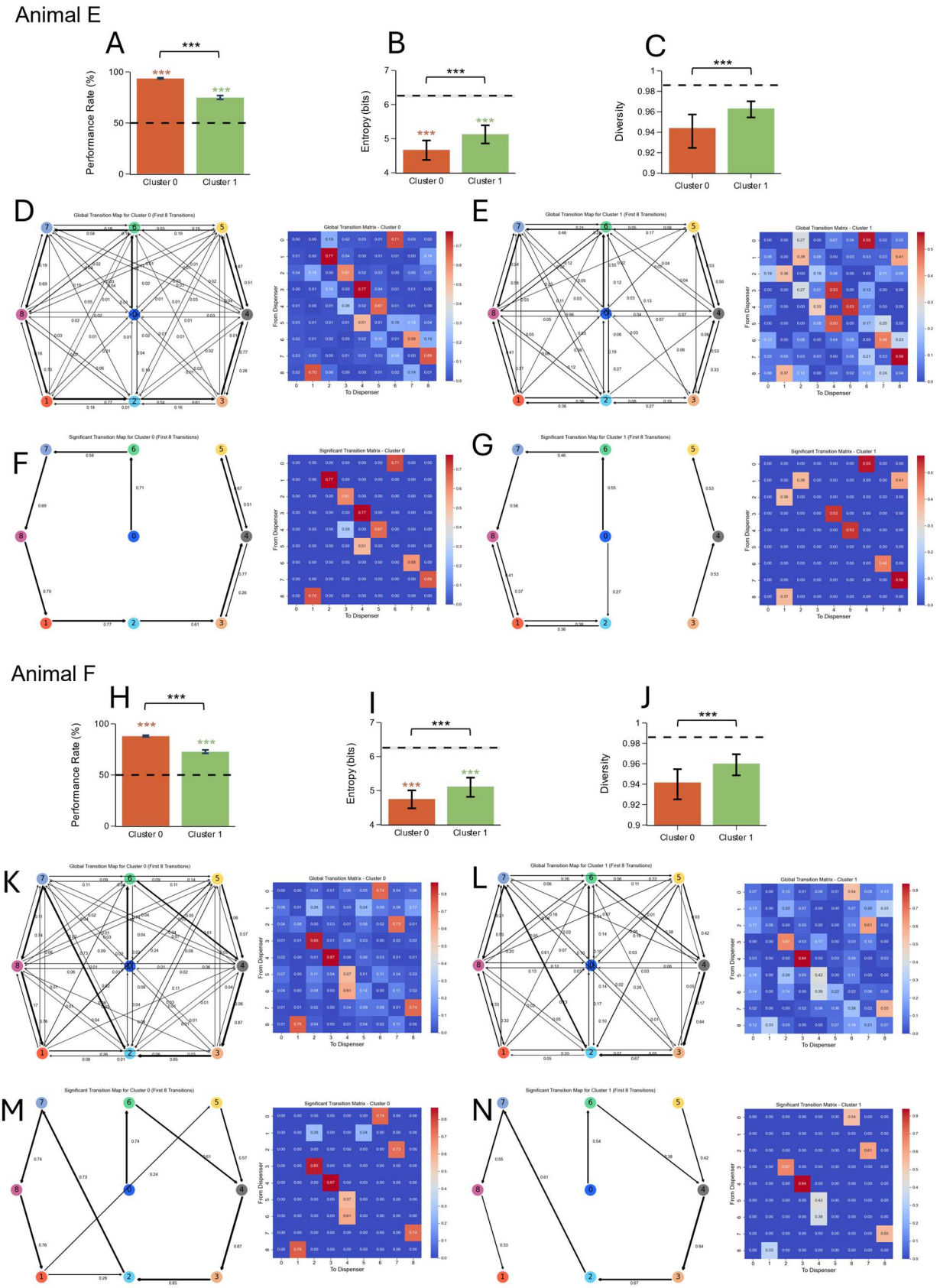

J), confirming that marmosets' behavior in both clusters deviated markedly from random exploration.

Figure 3: Clusters 0 and 1 reflect variations in efficiency within a shared behavioral framework
(A-G) Cluster 0 and 1 analysis for Animal E; (H-N) Cluster 0 and 1 analysis for Animal F, following the same conventions as Animal E.
A and H. Performance in the first eight choices across clusters 0 and 1. Bar plot showing the mean performance rate (% correct responses) for each cluster, computed over the first eight choices of each trial for Animal E (A) and Animal F (H). Error bars represent the SEM. The dashed line indicates the 50% threshold expected under random selection among nine possible options. Statistical analysis was performed using the Wilcoxon signed-rank test to compare each cluster's performance against the random performance, and the Mann-Whitney U test to compare performance between Clusters 0 and 1, with p-values corrected for multiple comparisons using the Bonferroni method. Significant results are indicated by asterisks (***p < 0.001). **B and I. Global entropy across clusters 0 and 1.** Bar plot showing the mean global entropy (in bits) for Clusters 0 and 1, with bootstrap-estimated 95% confidence intervals for Animal E (B) and Animal F (I). Error bars represent the 95% confidence intervals (CI) for the entropy values. The dashed black line represents the mean global entropy expected under a random transition model, with shaded regions indicating the 95% CI for random entropy. Statistical significance was assessed using a permutation test, with p-values corrected for multiple comparisons using the Bonferroni method. Significant results are indicated by asterisks (***p < 0.001). **C and J. Global transition diversity across clusters 0 and 1. Bar** plot showing the mean global transition diversity for Clusters 0 and 1, with bootstrap-estimated 95% confidence intervals for Animal E (C) and Animal F (J). Error bars represent the 95% confidence intervals (CI) for the global transition diversity values. The dashed black line represents the mean global diversity expected under a random transition model, with shaded regions indicating the 95% CI for random diversity. Statistical significance was assessed using a permutation test, with p-values corrected for multiple comparisons using the Bonferroni method. Significant results are indicated by asterisks (***p < 0.001). **D and K. Global transition map and matrix for cluster 0**. Directed graph representing all observed transitions between dispensers within the first 8 choices across all trials (left), averaged within each cluster for Animal E (D) and Animal F (K). Node positions correspond to dispenser locations, and arrow thickness is proportional to the probability of a transition occurring. Thicker arrows indicate more frequently used transitions, while thinner arrows represent less common paths. This visualization highlights the overall structure of movement patterns within each cluster. Global transition matrix (right) for Clusters 0 displaying the transition probabilities between all dispensers. Color intensity represents the strength of the transitions, with dark blue indicating low probabilities and dark red indicating high probabilities. These matrices show all observed transitions within each cluster, including both frequent and less frequent transition. **E and L. Global transition map and matrix for cluster 1**. Structure and visualization are identical to those in panel D but correspond to Cluster 1. The directed graph (left) represents all observed transitions between dispensers, while the transition matrix (right) shows the probabilities of these transitions. Node positions, arrow thickness, and color intensity follow the same conventions as in panel D.**F and M. Statistically significant transition map and matrix for cluster 0**. Directed graph (left) displaying only transitions that were significantly more frequent than expected under a uniform random model (p = 1/9) for Animal E (F) and Animal F (M). Statistical significance was determined using binomial tests with Bonferroni correction. Arrows indicate significant movement patterns, revealing key transitions that characterize structured behavior within each cluster. Thicker arrows represent transitions with higher probabilities, emphasizing dominant movement paths. Significant transition matrices for Cluster 0 (right) highlighting transitions that are significantly different from random chance. Color intensity in these matrices represents the strength of these statistically significant transitions, with dark red indicating strong preferences for specific transitions that consistently occurred more frequently than expected by chance. **G and N. Statistically significant transition map and matrix for cluster 1**. Structure and analysis are identical to those in panel F but correspond to Cluster 1. The directed graph (left) shows statistically significant transitions, while the transition matrix (right) highlights transitions that deviate significantly from random chance. Arrows and color intensity follow the same conventions as in panel F.

We then built transition matrices to quantify transition probabilities between locations and used transition maps to visualize how dispensers were sequentially connected. Global transition maps displayed all observed transitions, with arrow thickness proportional to transition probabilities (**Fig. 3D-E; K-L**), while significant transition maps highlighted transitions occurring significantly more often than expected by chance (binomial tests with Bonferroni correction; **Fig. 3F-G; 3M-N**).

Correlation analyses revealed a strong alignment in transition organization between clusters, indicating highly similar movement patterns (global matrices: Animal E: r=0.89 p<0.001; Animal F: r=0.91 p<0.001; significant matrices: Animal E: r=0.74 p<0.001; Animal F: r=0.96 p<0.001). Despite these strong correlations, Euclidean distances between transition matrices revealed notable differences in absolute transition probabilities (global matrices: Animal E: 0.90; Animal F: 0.84; significant matrices: Animal E: 1.92; Animal F: 0.72). These findings indicate that the transition matrices of the two clusters share a common structural framework, although there are differences in the exact distribution of transition probabilities that distinguish Cluster 0 from Cluster 1.

Overall, these results show that Clusters 0 and 1 do not reflect fundamentally different behavioral strategies, but rather variations in the degree of task precision and efficiency within a shared behavioral framework. Given this similarity, we pooled Clusters 0 and 1 for subsequent analyses of spatial learning.

Evolution of Performance and Global Transition Pattern Across Training Phases

We next sought to determine whether performance improvement was associated with changes in the organization of transition patterns. To investigate this, we divided the training sessions into six phases, each consisting of five sessions: the first ten sessions were divided into Beg 1 (S1–S5) and Beg 2 (S6–S10); the ten intermediate sessions into Int 1 (S11–S15) and Int 2 (S16–S20); and the last ten sessions into Last 1 (S21–S25) and Last 2 (S26–S30).

As expected, performance significantly improved across training phases, (**Fig. 4A**; **F**) calculated from the first 8 choices of each trial (Kruskal-Wallis; Animal E: $H = 11.656$, $p = 0.03$; Animal F: $H = 64.6$, $p < 0.001$).

In parallel, the global entropy of transitions (**Fig. 4B**;**G**) within the first eight choices significantly decreased over training phases (Permutation test; p<0,001 for all comparisons), providing evidence of a more structured task execution emerging over time in both animals. The progressive reduction in global entropy was closely associated with performance improvements (**Fig. 4C**;**H)**, as reflected by a strong and significant negative correlation between mean global entropy and mean performance across training phases (Animal E: $r = -0.88$, $p = 0.04$; Animal F: $r = -0.93$, $p = 0.01$). These results indicate a consistent relationship between entropy reduction and task performance improvements across training phases.

To further quantify this evolution, we examined the overlap index, which measures the similarity between global entropy distributions across training phases (with 0 indicating no similarity and 1 complete overlap) (**Fig. S4)**. For both animals, the low overlap between early and intermediate phases (Beg 1 vs. Int 2: Animal E: 0.15; Animal F: 0.004) reveals a clear shift in transition patterns during early training. However, overlap increased in later stages (Int 2 vs. Last 2: Animal E: 0.7; Animal F: 0.5), suggesting greater consistency and refinement of transition behaviors.

The global (**Fig. 4D;I**) and significant (**Fig. 4E;J**) transition maps offer additional insights into the refinement of transition behavior over training. Permutation-based correlation analyses (Bonferroni-corrected) confirmed that, for both types of matrices, the overall transition structure remained stable throughout training in both animals (**Fig. S4 B-C; H-I**). However, Euclidean distances highlighted substantial changes in individual transition probabilities, which progressively decreased over time, indicating a reduction in transition variability.

Together, these findings illustrate a progressive shift toward more structured and consistent transition behaviors over training. As performance improved, transition variability decreased, leading to more predictable and organized movement patterns.

Local Transition Analysis Uncovers Dispenser-Specific Variability Within a Globally Structured Transition Behavior

We next examined whether the global trends in transition organization were also reflected at the level of individual dispensers by quantifying local entropy (**Fig. S4 D;J**). For both animals, local entropy decreased significantly over training (Kruskal-Wallis; Animal E: $H = 12.6$, $p = 0.02$; Animal F: Kruskal-Wallis $H = 25.67$, $p < 0.001$), reflecting an increasing structuring of transitions at the individual dispenser level. Post-hoc comparisons with Bonferroni correction revealed significant decreases between early (Beg1) and late (Last 2) training phases (Animal E: $p=0.04$; Animal F: $p=0.03$), highlighting a marked reduction in transition variability at the dispenser level.

To assess the functional relevance of dispenser-level structuring, we examined the probability of errors following visits to individual dispensers—measuring the likelihood of making an

incorrect choice after leaving a specific location **(Fig. S4 E;K**). For both animals, error probability decreased significantly between early and late training phases (Kruskal-Wallis; Animal E: $H = 6.5$, $p = 0.01$; Animal F: $H = 7.6$, $p < 0.01$). Post-hoc comparisons with Bonferroni correction revealed a marked and significant reduction in error probability between early (Beg 1) and late (Last 2) training phases ($p<0.01$ for both animals). Notably, we observed a strong positive correlation between mean local entropy and mean error probability across training phases (Animal E: $r = 0.9$, $p < 0.01$; Animal F: $r = 1$, $p < 0.001$) **(Fig. S4 F;L**), indicating that increased structuring at the local level was closely linked to improved task performance.

To assess whether the structuring of transition patterns at the local level was spatially homogeneous, we compared local entropy values across individual dispensers relative to a baseline distribution generated from 1,000 bootstrap-sampled random transitions (mean = 2.65 bits, 95% CI: 2.15–2.98). While many dispensers showed entropy values significantly below this baseline, indicating consistent transition structuring, others did not differ from chance. This reveals that the reduction in transition variability over training was not uniform, with some dispensers supporting more predictable navigation patterns than others.

Together, the local analysis reinforces the global findings by confirming a progressive structuring of transitions over training, which is closely linked to improved performance. However, it also reveals notable heterogeneity among dispensers, with some exhibiting more variable transition patterns than others. This variability suggests that certain locations act as flexible transition points, whereas others are integrated into more rigid and predictable transition sequences. These findings highlight the fine-scale organization of spatial navigation strategies, demonstrating that while global trends reflect overall structuring, local analysis uncovers location-specific adaptations that shape task execution.

Marmoset Transition Patterns show Local Predictability but Global Flexibility

We next sought to determine whether the increasing structuring of transition patterns over time reflected the adoption of rigid, repetitive strategies or the emergence of more flexible, probabilistic preferences. To address this, we examined whether successful performance in error-free trials consistently relied on the same transition behavior or if multiple transition patterns could lead to success, indicating a degree of variability in strategy use.

We applied a Markov chain model to assess the predictability of transitions at both local and global levels. Markov chain models are well-suited for capturing sequential dependencies, as they estimate the likelihood of transitioning from one state (dispenser) to another based solely on the current state. This allowed us to evaluate the model's ability to predict individual transitions (local level) as well as entire sequences of dispenser visits (global level). Importantly, the model was trained solely on error-free trials to investigate the relationship between behavioral structuring and successful task execution. Its predictive performance was then compared to a Random Baseline model, where all transitions were assumed equally probable.

Animal E

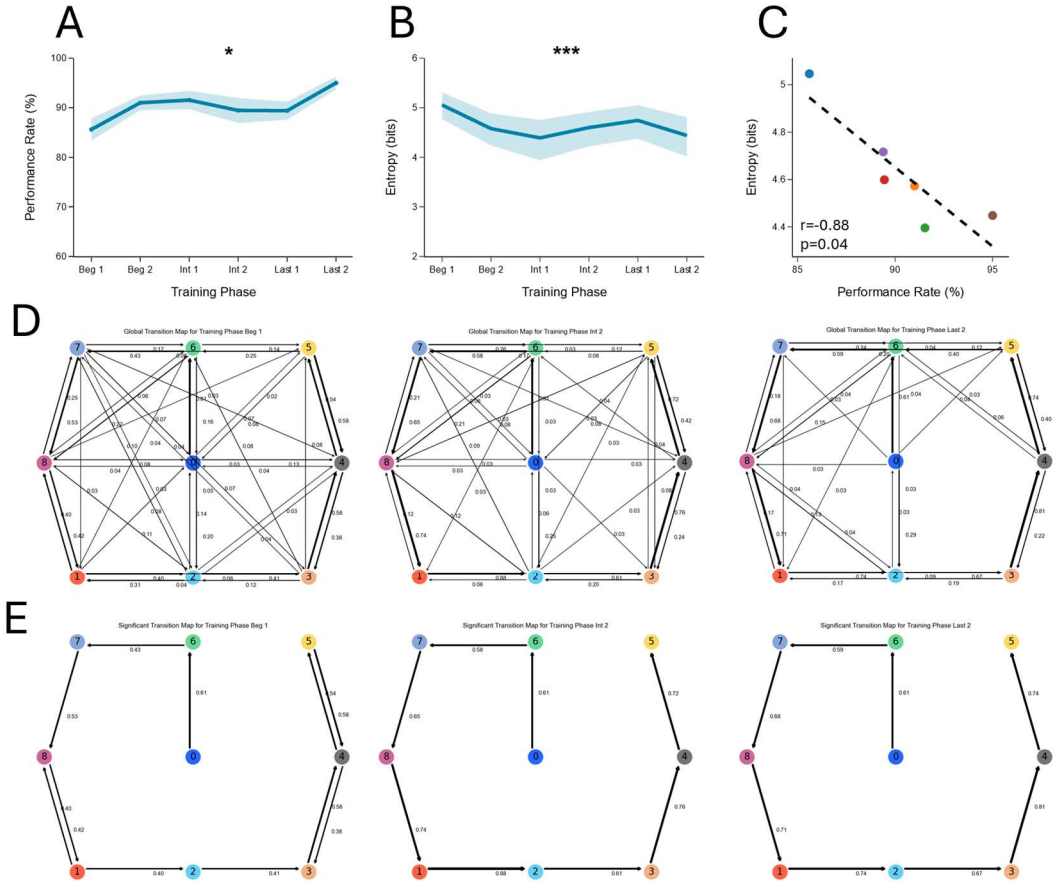

Animal F

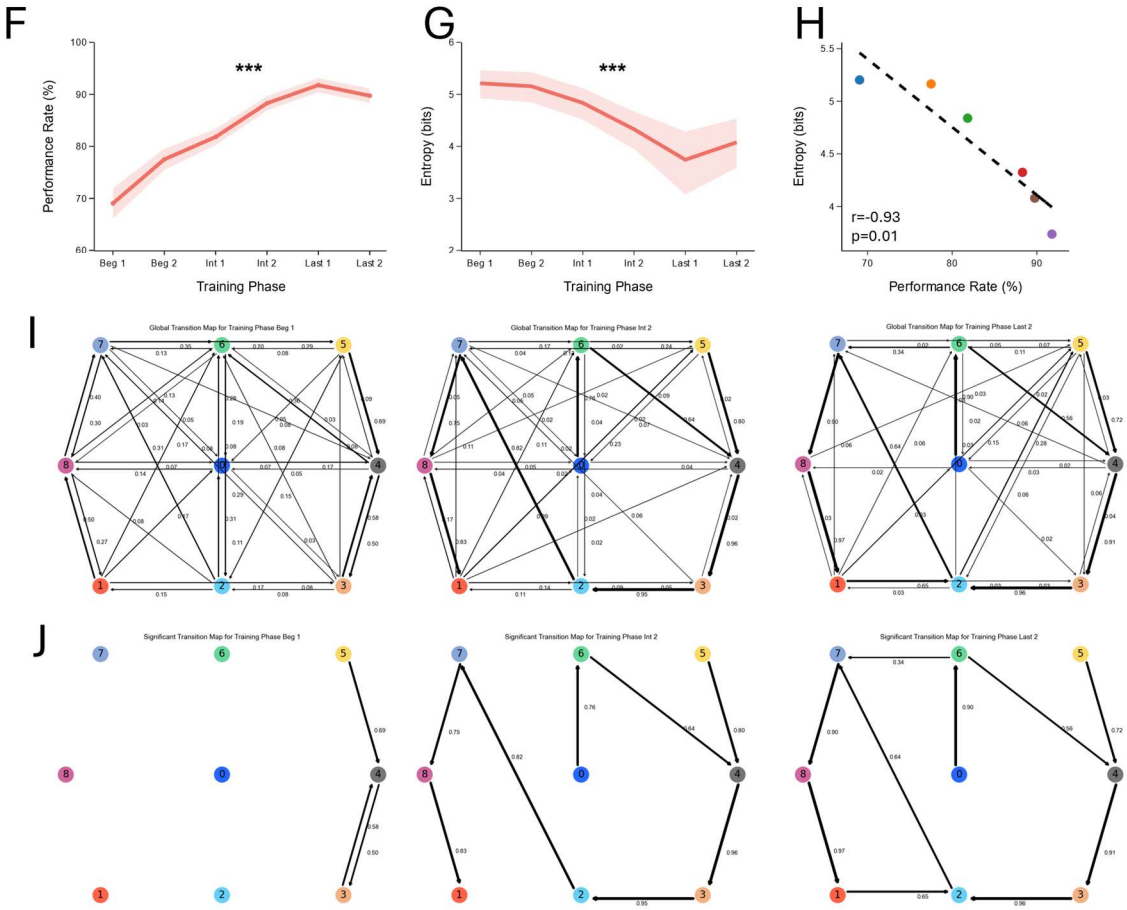

Figure 4: Evolution of Performance and Transition Pattern Across Training Phases.
(A-E) Different phases of training analysis for Animal E; (F-J) Different phases of training analysis for Animal F, following the same conventions as Animal E.
A and F. Performance in the first 8 choices across training phases. Line plot showing the mean performance rate (%) within the first eight choices of each trial, plotted across six distinct training phases for Animal E (A) and Animal F (F). The solid line represents the mean performance rate, and the shaded area shows the standard error of the mean (SEM). Statistical analysis was performed using the Kruskal-Wallis test followed by Dunn's post-hoc test with Bonferroni correction. Significant p-values from the Kruskal-Wallis test are marked with asterisks: *** $p < 0.001$, ** $p < 0.01$, * $p < 0.05$. **B and G. Evolution of global entropy across training phases**. Line plot showing the evolution of mean global entropy (in bits) across different training phases. The points represent the mean global entropy values, while the shaded area indicates the 95% confidence interval (CI) for each training phase. Statistical analysis was performed using a permutation test with Bonferroni correction. Significant p-values are marked with asterisks: *** $p < 0.001$, ** $p < 0.01$, * $p < 0.05$. **C and H. Correlation between performance rate and global entropy.** Scatter plot showing the relationship between the performance rate (in percentage) and entropy (in bits) across different training phases. Each point represents the data for a specific training phase, color-coded according to the training phase. A dashed black line represents the linear regression fit, illustrating the overall trend. Pearson correlation between performance and entropy was calculated, with Bonferroni correction applied for multiple comparisons. **D and I. Global transition maps.** Directed graph representing all observed transitions between dispensers within the first 8 choices across all trials, averaged for the different training phases of Animal E. The maps show transitions for the following periods: Beg 1 (S1-S5) on the left, Int 2 (S16-S20) in the middle, and Last 2 (S26-S30) on the right. Node positions correspond to dispenser locations, and arrow thickness represents the probability of a transition occurring. Thicker arrows indicate more frequently used transitions, while thinner arrows represent less common paths. **E and J. Statistically significant transition map.** Directed graph displaying only transitions that were significantly more frequent than expected under a uniform random model ($p = 1/9$). Statistical significance was determined using binomial tests with Bonferroni correction. The maps show significant transitions for the following periods: Beg 1 (S1-S5) on the left, Int 2 (S16-S20) in the middle, and Last 2 (S26-S30) on the right. Arrows indicate significant movement patterns, revealing key transitions that characterize structured behavior within each training phase. Thicker arrows represent transitions with higher probabilities, emphasizing dominant movement paths.

The Markov model demonstrated strong performance in predicting local transitions (**Fig. 5A-D**), with an average prediction accuracy of 79.6% ± 7.8% (CI 95%) for Animal E and 84.75% ± 2.7% (CI 95%) for Animal F. Both values exceeded the Random Baseline model, which achieved 10.5% ± 1.8% (IC 95%) for Animal E and 9.0% ± 3.5% (CI 95%) for Animal F. Wilcoxon signed-rank tests confirmed that these differences were statistically significant ($p < 0.01$ for both animals). These results highlight the model's ability to predict transitions based on sequential dependencies, showing that a Markovian framework can provide a robust representation of the animals' transitions at the local level.

To evaluate whether local transition patterns extended to full-sequence prediction, we examined the model's ability to capture larger-scale behavioral patterns by iteratively selecting the most probable successive transitions predicted by the Markov model (**Fig. 5E-F**). While accuracy decreased when predicting full sequences compared to individual transitions, the Markov model still outperformed the Random Baseline. The average sequence accuracy was 57.1% ± 13.8% (CI 95%) for Animal E and 54.5% ± 6.5% (CI 95%) for Animal F, whereas the Random Baseline consistently achieved 0% accuracy. Wilcoxon signed-rank tests confirmed the Markov model's superior performance was statistically significant ($p < 0.01$ for both animals).

Overall, these results demonstrate that while individual transitions are predictable, complete sequences exhibit a degree of flexibility. The Markov model performed well in predicting local transitions during error-free trials, but its accuracy declined when applied to entire sequences, indicating that the animals do not follow a single, fixed sequence. Nonetheless, predicting more than 50% of complete sequences indicates dominant transition patterns in successful trials, albeit with variability in execution.

Predictability of Local and Global Transition Patterns Evolves Dynamically Across Training Phases

While the Markov model demonstrated strong predictability for local transition patterns and some flexibility at the sequence level in error-free trials, how this predictability evolved at both local and global levels throughout training remained unclear. We next examined how transition

patterns changed across successive training phases, specifically assessing the Markov model's ability to predict local transitions and global sequences within error-free trials.

The predictive accuracy of the model was compared against a Random Baseline in each phase. A Kruskal–Wallis test was used to evaluate changes in the Markov model's performance over training phases. In parallel, Wilcoxon signed-rank tests compared the model's accuracy to the Random Baseline in each phase, with Bonferroni correction applied to all p-values.

Error-free trials appeared at different training phases in each animal (Animal E: Beg 1; Animal F: Int 1). However, once error-free trials emerged, both animals exhibited a similar trajectory in terms of local transition predictability (**Fig. 5G,K;I,M**).

Initially, the Markov model did not significantly outperform the Random Baseline in either Animal E (Beg 1: 33.3% ± 12.9% (95% CI), $p > 0.05$) or Animal F (Int 1: 50.0% ± 0.0% (95% CI), $p > 0.05$), reflecting a high degree of unpredictability in local transition behavior. As training progressed, the Markov model's accuracy improved significantly for both animals (Kruskal-Wallis; Animal E: $H=22.3$, $p<0.001$; Animal F: $H= 16.7$, $p < 0.001$), consistently surpassing the Random Baseline in all subsequent phases (Wilcoxon signed-rank test, $p < 0.05$ for all comparisons). Accuracy increased significantly across training phases, peaking at 86.8% ± 12.9% (95% CI) in Int 1 for Animal E and 96.3% ± 3.7% (95% CI) in Last 1 for Animal F, before slightly declining in subsequent phases.

These findings show that error-free trials in early training phases involved near-random local transitions with no strong preference for specific dispenser patterns. Over time, transitions became more predictable, reflecting the emergence of stable strategies at the local level. However, after reaching a peak, accuracy declined, indicating that these local structured patterns were not fully maintained in the last training phases.

We then examined the Markov model's ability to predict complete sequences of dispenser visits across training phases, shifting our focus to the global level (**Fig. 5H,L;J,N**).

Initially, the Markov model failed to predict any complete sequences for Animal E (Beg 1: 0%) and Animal F (Int 1: 0%) reflecting the high variability in the sequences used by both animals. As training progressed, sequence prediction accuracy improved significantly (Kruskal-Wallis; Animal E: $H = 17.8$, $p < 0.01$; Animal F: $H = 22.5$, $p < 0.001$), peaking at 70% ± 26.1% (95% CI) in Int 1 for Animal E and 85% ± 14.96% (95% CI) in Last 1 for Animal F, significantly surpassing the Random Baseline (Wilcoxon signed-rank test, $p < 0.01$). However, accuracy declined sharply in the final training phase (Last 2), dropping to 45% ± 22.8% (95% CI) for Animal E and returning to 0% for Animal F, marking a notable decrease in sequence predictability at the end of training.

In conclusion, the global-level predictability of the Markov model followed a non-linear trajectory, increasing steadily to a peak where sequences were highly predictable before declining in later phases. These results indicate that the animals' sequence use in error-free trials evolved across training phases, alternating between periods of high predictability and greater variability.

Together, the local and global analyses highlight the dynamic evolution of transition behaviors across training phases. While local transition patterns became increasingly structured, the flexibility at the global level remained evident, with the Markov model showing both predictable patterns and variability in sequence use. The interplay between predictability at the local level and flexibility at the global level underscores the adaptive nature of marmosets' navigation

strategies, reflecting both the refinement of task execution and the retention of flexibility throughout training.

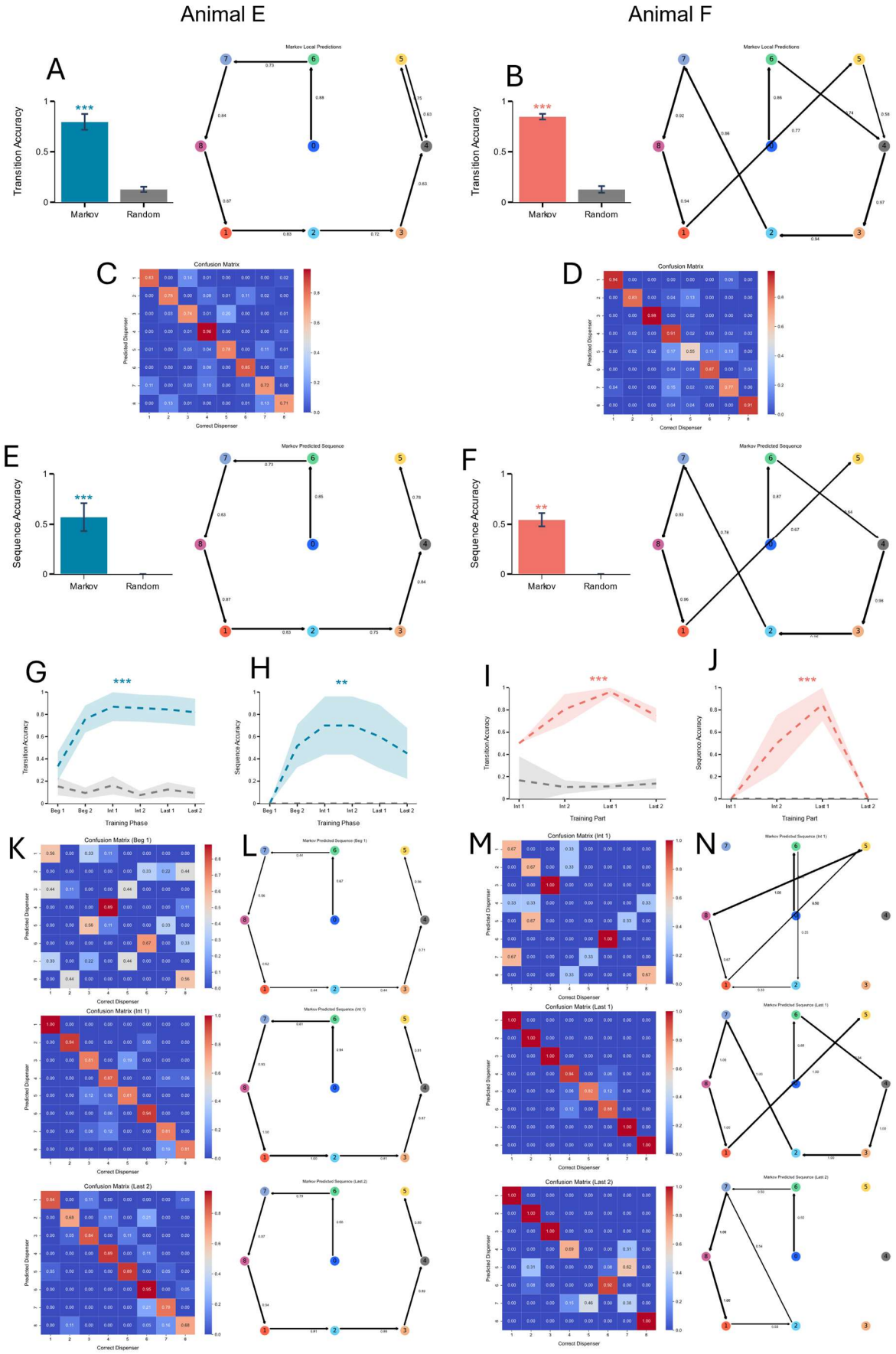

Figure 5: Markov's model accuracy at both local and global scales
A-B. Markov model's transition accuracy and Transition map depicting local predictions from Markov model (Left) Bar plot showing the mean transition accuracy (across cross-validation folds) for the Markov model and the random baseline. Error bars represent the 95% confidence interval (CI). Statistical analysis was performed using the Wilcoxon signed-rank test with Bonferroni correction to assess whether differences in accuracy between the two models were statistically significant. Significant p-values are marked with asterisks: *** $p < 0.001$, ** $p < 0.01$, * $p < 0.05$. (Right) Directed graph showing the most likely next dispenser state based on transition probabilities learned from the training data. Each node corresponds to a dispenser, and edges represent the most probable transitions to the next dispenser. Arrow thickness is proportional to transition probability, with node positions reflecting their physical layout. Analysis for Animal E (panel A) and for Animal F (panel B).**C-D. Normalized average confusion matrix for the Markov model**. Confusion matrix displaying predicted versus actual dispenser choices with the color scale ranging from dark blue (lower frequencies) to red (higher frequencies). The matrix rows have been normalized so that each row shows the distribution of predictions for a given dispenser. The diagonal cells indicate the proportion of correct predictions, highlighting the performance of the Markov model. **E-F. Markov model's sequence accuracy and Transition map depicting sequence prediction from the Markov model**(Left) Bar plot showing the mean sequence accuracy (across cross-validation folds) for the Markov model and the random baseline. Error bars represent the 95% confidence interval (CI). Statistical analysis was performed using the Wilcoxon signed-rank test with Bonferroni correction to assess whether differences in accuracy between the two models were statistically significant. Significant p-values are marked with asterisks: *** $p < 0.001$, ** $p < 0.01$, * $p < 0.05$. (Right) Directed graph illustrating the most probable sequence, from state 0 through up to eight transitions, predicted by the Markov model. Each node represents a dispenser, and edges indicate the most likely transitions. Analysis for Animal E (panel E) and for Animal F (panel F).**G and I. Markov model's transition accuracy across training phases.** Line plot showing the mean transition accuracy (across cross-validation folds) for the Markov model and the random baseline across the six training phases. The dashed lines represent the mean accuracy, with each point corresponding to the average accuracy for the respective training phase. The shaded areas represent the 95% confidence intervals (CI). Statistical analysis was performed using the Wilcoxon signed-rank to compare the Markov model against the Random model and Kruskal-Wallis with Dunn's post-hoc test to compare the evolution of the Markov model across training phases. All p-values were corrected using the Bonferroni method. Significant p-values are marked with asterisks: *** $p < 0.001$, ** $p < 0.01$, * $p < 0.05$. Analysis for Animal E (panel G) and for Animal F (panel I). **H and J. Markov model's sequence accuracy across training phases**. Line plot showing the mean sequence accuracy (across cross-validation folds) for the Markov model and the random baseline across the six training phases. The dashed lines represent the mean accuracy for both the Markov model and the random baseline, with shaded areas representing the 95% confidence intervals (CI). Statistical analysis was performed using the Wilcoxon signed-rank to compare the Markov model against the Random model and Kruskal-Wallis with Dunn's post-hoc test to compare the evolution of the Markov model across training phases. All p-values were corrected using the Bonferroni method. Significant p-values are marked with asterisks: *** $p < 0.001$, ** $p < 0.01$, * $p < 0.05$. Analysis for Animal E (panel H) and for Animal F (panel J).**K and M. Confusion matrices for the Markov model during different training phases**. Confusion matrices showing predicted versus actual dispenser choices during the Beg 1 (S1-S5) (top), Int 2 (S16-S20) (middle), and Last 2 (S26-S30) (bottom) training phases. Each matrix cell represents the proportion of times a given dispenser was predicted for each actual dispenser. Darker cells indicate higher prediction frequencies, showcasing the model's performance in predicting dispenser choices across different training phases. Analysis for Animal E (panel K) and for Animal F (panel M). **L and N. Transition maps for each training phase depicting sequence prediction from the Markov model**. Directed graphs illustrating the most probable sequence, from state 0 through up to eight transitions, predicted by the Markov model during the Beg 1 (S1-S5) (top), Int 2 (S16-S20) (middle), and Last 2 (S26-S30) (bottom) training phases. Each node represents a dispenser, and edges indicate the most likely transitions. Analysis for Animal E (panel L) and for Animal F (panel N).

Sequences of Dispenser Visits Are Variable but Share Core Transitions

To further investigate the variability of complete sequences in successful trials, we analyzed the number of unique sequences used by each animal and assessed their relative frequency (**Fig. 6A;C**). We identified 22 unique sequences for Animal E and 11 for Animal F. Despite this diversity, the sequences were not used equally, with a dominant sequence emerging for each animal, accounting for 65.1% of the sequences in successful trials for Animal E and 56.5% for Animal F.

To quantify sequence variability, we computed the normalized Shannon diversity index, which captures both the number of unique sequences and their relative distribution. This index ranges from 0 to 1, where 0 indicates no variability (i.e. a single sequence is used exclusively) and 1 reflects maximal diversity in sequence use. We found a Shannon index of 0.59 for Animal E and 0.66 for Animal F, confirming that both animals exhibited variability in their sequence selection to complete the task.

We then examined sequence similarity by analyzing common transitions (**Fig. 6B,E,F;D,G,H**). For each sequence, we extracted the set of transitions (i.e. pairs of consecutive dispensers) and computed the Jaccard similarity index between them. This measure reflects the proportion of shared transitions relative to the total number of unique transitions, with values ranging from 0 (no similarity) to 1 (complete similarity).

For Animal E, the overall mean Jaccard similarity between sequence pairs was 0.54 ± 0.006. Notably, 54.7% of sequence pairs shared at least 50% of their transitions, while 40.4% exhibited a similarity between 60% and 70%, and 33.8% of pairs were identical (100% overlap), indicating that a substantial proportion of sequences followed similar structural patterns. Additionally, 7 transitions appeared in more than 70% of the sequences, highlighting dominant patterns in the sequence of dispenser visits.Similarly, for Animal F, the mean Jaccard similarity was 0.58 ± 0.01. In this case, 56.9% of sequence pairs shared at least 50% of transitions, 38.4% had a similarity between 60% and 70%, and 32.6% were identical. Furthermore, 5 transitions were found in more than 75% of the sequences, reinforcing the structured nature of dispenser visit patterns in successful trials.

These findings indicate that while animals predominantly rely on a dominant sequence in most of the error-free trials, some variability exists in sequence used. However, the high proportion of sequences exhibiting moderate to high similarity indicate that animals rely on a core set of transitions between dispensers, even when exploring alternative sequences.

Dynamics of Sequence Diversity and Similarity

We next sought to investigate how both sequence diversity and similarity evolved across training phases. By examining how these aspects changed throughout the task, we aimed to gain insights into how animals adapt their behavior and transition patterns during error-free trials as training progressed.

We first examined the evolution of sequence variability by analyzing the change in the normalized Shannon diversity index over training phases (**Fig.6 I;J**). For both animals, we observed a non-linear U-shape trend. To quantify this trajectory, we fitted a quadratic model to the normalized diversity values. For Animal E, the quadratic model explained a substantial portion of the variance ($R^2 = 0.96$, $p<0.01$), confirming the significance of the U-shaped pattern in sequence diversity. For Animal F, the quadratic fit also captured the trend ($R^2 = 0.86$) and provided a much better explanatory power than a linear model ($R^2 = 0.4$). However, because error-free trials were only present in 4 training phases for this animal, the quadratic model did not reach statistical significance ($p = 0.3$). Despite this, the strong increase in R^2 compared to the linear model suggests that a non-linear trajectory is likely present in both animals.

To further investigate this trend, we analyzed the frequency of the dominant sequence across training phases (**Fig. 6K; L**). For both animals we observed an inverted U-shaped pattern. These results indicate that both animals initially exhibited variability in sequence use, with the dominant sequence becoming increasingly prevalent over training phases before declining in the last phases. Additionally, a negative correlation (**Fig. 6K; L**) was found between dominant sequence frequency and the normalized Shannon diversity index (Animal E: $r = -0.95$, $p < 0.01$; Animal F: $r = -0.95$, $p = 0.05$), confirming that as the dominant sequence became more frequent, overall sequence diversity decreased, and vice versa.

To explore the evolution of sequence similarity across training phases, we computed the Jaccard similarity index between all pairs of sequences within each training phase (**Fig. 6M; N**). For both animals, sequence similarity between pairs of sequences changed significantly over training phases (Kruskal-Wallis; Animal E: $H = 50.38$, $p < 0.001$; Animal F: $H = 102.74$, $p < 0.001$). Sequence similarity was initially low, reflecting high sequence variability in the early training phases. As training progressed, sequence similarity increased progressively, reaching a peak for both Animal E (Int 1: 0.66±0.03) and Animal F (Last 1: 0.89±0.013). While sequence similarity decreased significantly in the subsequent phases (Dunn post-hoc tests; Animal E: Int 1 vs Last 2, $p<0.05$; Animal F: Last 1 vs Last 2, $p<0.001$), it remained significantly higher than in the initial phases (Dunn post-hoc tests; Animal E: Beg 1 vs Last 2, $p<0.001$; Animal F: Int 1 vs Last 2, $p<0.05$). These results indicate that, as training progressed, the sequences used in

error-free trials within each training phase increasingly shared common transitions between dispensers, reflecting a growing consistency in the animals' transition patterns.

These findings reveal that the animals' use of sequences evolved dynamically over the course of training. Initially, there was high variability in sequence use, with low similarity between sequences. As training progressed, however, dominant sequences emerged. In the final training phase, although sequence diversity increased, sequence similarity remained high, indicating that despite greater variability, the sequences continued to share many common transitions, highlighting a more structured approach to task execution even when exploring alternative sequences.

Marmosets' Shift from Novel to Reused Sequences Across Training Phases

While sequence diversity and similarity evolved throughout training, it remains unclear whether the observed variability in sequence use is due to the continuous introduction of entirely new sequences or the flexible reuse of sequences learned earlier in training. To investigate this, we examined the relative contributions of novel versus reused sequences in each training phase. By investigating whether the variability in sequence use is driven by the introduction of new strategies or the use of previously learned ones, we aim to better understand how animals balance exploration and exploitation of learned behavior across different phases of training.

To do so, we analyzed two complementary measures to quantify how sequence use evolved over training: the New Sequence Ratio (NSR) and the Reused Sequence Ratio (RSR). The NSR quantifies the extent to which new sequences are used in each training phase. This ratio is calculated by dividing the number of new sequences (i.e. those not previously used by the animal) by the total number of unique sequences in the given phase. A high NSR suggests that the animal is actively exploring and introducing a large number of novel strategies, while a low NSR indicates less exploration of novel strategies and a greater reliance on sequences already used.

In parallel, the RSR measures the proportion of sequences in each phase that were already present in previous phases. This metric is calculated by dividing the total number of repetitions of previously used sequences by the total number of sequences in the current phase. A high RSR indicates that the animal tends to repeat previously used sequences more frequently, demonstrating a strong reliance on familiar strategies. In contrast, a low RSR suggests that the animal is less reliant on past sequences and continues to explore new strategies, using a wider variety of novel sequences.

Both Animal E and Animal F displayed a clear pattern in their use of new and previously learned sequences across training phases (**Fig. 6O-R)**. In the early stages of training, both animals exhibited relatively high NSR, reflecting a strong focus on exploring and introducing new sequences. However, as training progressed, the NSR gradually decreased for both animals, indicating a shift towards increased reliance on previously used sequences. This trend was confirmed by the RSR, which progressively increased throughout the training phases. In the later phases, a substantial proportion of the sequences used had already been encountered in earlier phases, suggesting a greater reliance on learned sequences.

Notably, the RSR exhibited a non-linear pattern, reflecting a complex shift in the animals' use of previously learned sequences. Additionally, a negative correlation was found between the RSR and the Shannon diversity index (Animal E: $r=-0.83$, $p<0.05$; Animal F: $r=-0.93$, $p=0.07$), indicating that as the animals reused more sequences, the diversity of their strategies decreased. In contrast, the NSR showed no significant correlation with the Shannon diversity index (Animal E: $r=0.71$, $p=0.1$; Animal F: $r=-0.6$, $p=0.4$).

These findings demonstrate a shift from the introduction of new sequences to the reuse of previously learned ones, highlighting a changing balance between exploration of new sequences and exploitation of learned behaviors, as the animals progress through different phases of training.

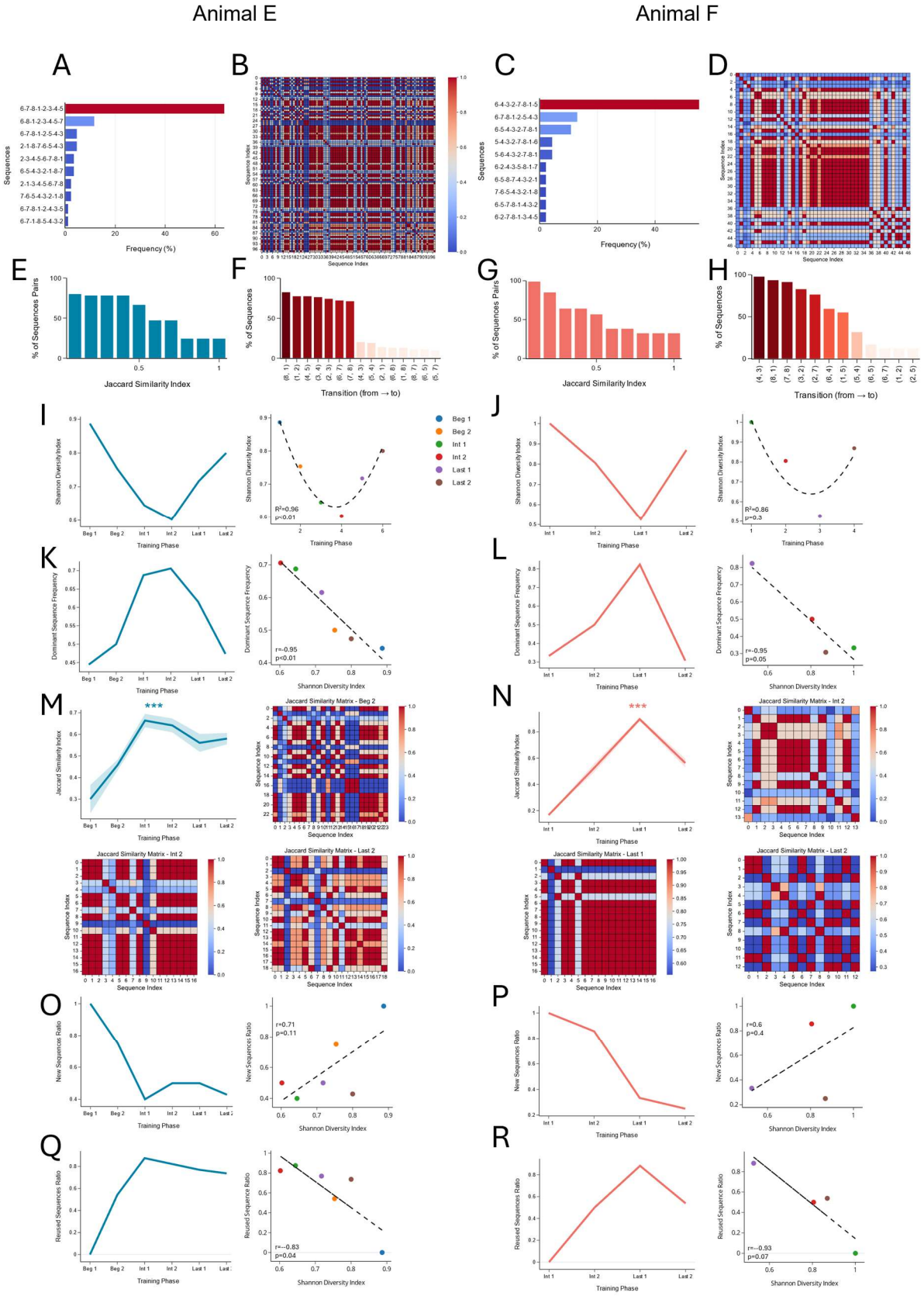

Figure 6: Analysis of Sequence Diversity and Similarity
A and C. Frequency of unique sequences within error-free trials. Horizontal bar plot displaying the top 10 most frequent transition sequences observed during error-free trials. Sequences are sorted in descending order of frequency, with percentages representing their relative occurrence within these trials. Analysis for Animal E (panel A) and for Animal F (panel C).**B and D. Jaccard Similarity Matrix of sequences**. Heatmap representing the Jaccard similarity index between different sequences in error-free trials. Each cell quantifies the degree of overlap between two sequences, with values ranging from 0 (no shared elements) to 1 (identical sequences). The color scale visually indicates similarity levels, where warmer colors denote higher similarity and cooler colors indicate lower similarity. This matrix provides insight into the structural relationships among sequences, helping to identify common or distinct patterns. Analysis for Animal E (panel B) and for Animal F (panel D).**E and G. Distribution of sequence pair similarities**. Bar plot illustrating the distribution of Jaccard similarity indices among sequence pairs in error-free trials. The x-axis represents the Jaccard similarity index (ranging from 0.1 to 1.0), while the y-axis indicates the percentage of sequence pairs with similarity values equal to or greater than each threshold. This visualization highlights the proportion of sequences sharing structural similarities, offering insights into the overall homogeneity or diversity of sequences within these trials. Analysis for Animal E (panel E) and for Animal F (panel G). **F and H. Most common transitions across error-free trials**. Bar plot displaying the most frequent transitions observed across all sequences in error-free trials. Each bar represents a specific transition (from one dispenser to another), with its height indicating the percentage of sequences containing that transition. The red color gradient reflects the relative frequency, where darker shades represent higher occurrence rates. The x-axis lists the transitions in descending order of frequency, while the y-axis shows the percentage of sequences in which each transition appears. Analysis for Animal E (panel F) and for Animal F (panel H). **I-J. Evolution and quadratic regression of sequence diversity across training phases**. (Left) Line plot displaying the normalized Shannon diversity index of error-free sequences across different training phases. Higher values reflect greater sequence diversity, whereas lower values indicate more repetitive patterns. (Right) Scatter plot displaying the normalized Shannon diversity index across training phases, with the points color-coded according to the training phase. The dashed line represents the best-fit quadratic model, capturing the trend in sequence diversity over time. Statistical significance is reported through the R^2 and p-value of the model. Analysis for Animal E (panel I) and for Animal F (panel J). **K-L. Frequency of dominant sequence and correlation with the sequence diversity**. (Left) Line plot illustrating the dominant sequence frequency, i.e the proportion of error-free trials in which the most frequently used sequence appears, across training phases. Higher values suggest increasing reliance on a specific pattern, whereas lower values indicate greater sequence variability. (Right) Scatter plot illustrating the relationship between the Shannon diversity index and the frequency of the dominant sequence across training phases. Points are color-coded by training phase. The dashed regression line highlights the trend, with the Pearson correlation coefficient (r) and p-value reporting the statistical association. Analysis for Animal E (panel K) and for Animal F (panel L).**M-N. Evolution of Jaccard similarity index across training phases and Jaccard similarity matrices by training phase**. (Top-Left) Line plot showing the evolution of the mean Jaccard similarity index across training phases, with shaded areas representing the SEM. Statistical analysis was performed using the Kruskal-Wallis test, followed by Dunn's post-hoc test with Bonferroni correction for pairwise comparisons. Significant p-values are marked with asterisks: *** $p < 0.001$, ** $p < 0.01$, * $p < 0.05$. Heatmaps representing the Jaccard similarity index between sequences during three different training phases. Each matrix shows the degree of overlap between sequences, with values ranging from 0 (no shared elements) to 1 (identical sequences). The color scale visually highlights similarity patterns, providing insights into sequence consistency within each phase. Analysis for Animal E (panel M) and for Animal F (panel N). **O-P. Evolution of new sequences ratio across training phases and correlation with the sequence diversity**. (Left) Line plot displaying the New Sequences Ratio (NSR) across training phases. This ratio represents the proportion of sequences in each phase that were never used in any previous phase. A high NSR indicates greater exploration, while a low NSR suggests reliance on previously encountered patterns or phase-specific behaviors. (Right) Scatter plot showing the relationship between the Shannon diversity index and the New Sequences Ratio (NSR) across training phases. Each point represents a training phase, color-coded accordingly. The dashed regression line represents the best-fit linear regression, with Pearson correlation coefficient (r) and p-value indicating statistical significance. Analysis for Animal E (panel O) and for Animal F (panel P). **Q-R. Evolution of reused sequence ratio across training phases and correlation with the sequence diversity.** (Left) Line plot displaying the Reused Sequence Ratio (RSR) across training phases, representing the proportion of sequences in each phase that were already used in earlier phases. A high RSR suggests a preference for previously learned sequences, whereas a low RSR indicates a shift toward novel or phase-specific sequences. (Right) Scatter plot showing the relationship between the Shannon diversity index and the Reused Sequence Ratio (RSR) across training phases. Colors indicate different training phases. The dashed line represents the linear regression fit, with Pearson correlation coefficient (r) and p-value indicating the strength and significance of the relationship. Analysis for Animal E (panel Q) and for Animal F (panel R).

Discussion

Spatial memory is a core cognitive function that enables animals to efficiently track and retrieve information about their environment, thus optimizing foraging and navigation [1]. While extensive rodent research has revealed fundamental principles of spatial memory, how these mechanisms emerge in freely moving non-human primates (NHPs) remain less understood. In the present study, we address this gap by implementing a semi-naturalistic, unconstrained paradigm to investigate how common marmosets (*Callithrix jacchus*) progressively refine their navigation behaviors over repeated experience in a self-guided foraging task.

Unlike classical paradigms that impose rigid pathways or strong constraints [26,27] our setup allowed marmosets to explore spontaneously in an ecologically valid environment. This approach better approximates the complexity of wild conditions than smaller, highly controlled

laboratory settings, yet still permits detailed, quantitative analyses of performance and trajectory [28–30].Through a longitudinal assessment, we observed that marmosets do not rely on innate, fixed navigation behaviors but instead transition from an initial phase of broad exploration to increasingly structured and memory-guided strategies over time.

Our results demonstrate that spatial learning in marmosets is characterized by a progressive refinement of navigation strategies. Over time, performance improves spontaneously, reflecting the development of spatial working memory. This learning process is accompanied by an increasing structuring of navigation behavior, with dispensers being visited in a more predictable manner. However, despite this growing regularity, marmosets maintain a degree of flexibility, adjusting their routes dynamically rather than following rigidly fixed paths. This balance between structure and adaptability highlights the sophistication of their spatial navigation. These findings provide new insights into how spatial memory develops in NHPs, revealing an adaptive learning process that balances structure and flexibility—a hallmark of efficient spatial cognition.

Experience-Driven Improvements in Spatial Working Memory

A central finding is that marmosets demonstrated a progressive improvement in performance across training sessions, as evidenced by a significant reduction in total errors. If their choices had been purely driven by random exploration, error rates would have remained stable over time. Instead, the observed decline in both repetition and rule errors suggests that marmosets were actively refining their ability to track previously visited dispensers and maintain task structure—two key functions of spatial working memory. In contrast, omission errors followed a different trajectory, indicating that they were likely linked to motivational factors rather than deficits in memory.

To further dissect performance variability, we applied clustering analyses based on task engagement. This approach revealed distinct behavioral profiles: two clusters (Clusters 0 and 1) reflected engaged task execution, whereas the remaining two (Clusters 2 and 3) indicated disengagement. Crucially, only the engaged clusters exhibited performance improvements over training, reinforcing the idea that spatial memory refinements were contingent upon active task engagement. This distinction is especially important in neuroethological research, where natural fluctuations in motivation and attention can obscure cognitive effects. By isolating trials in which animals were demonstrably engaged, we obtain a more precise measure of memory-driven learning.

Unlike previous studies that primarily assessed final performance without tracking the full learning trajectory[24], our longitudinal approach—combined with engagement-based clustering—provides a nuanced understanding of how spatial working memory develops over time. Notably, this improvement emerged without explicit instruction or corrective feedback, emphasizing that marmosets refine their spatial memory intrinsically through repeated experience. This observation aligns with other marmoset tasks[31] and rodent studies [10,27,32,33] indicating a conserved, experience-driven refinement of memory-based navigation across species.

By integrating error analysis with task engagement clustering, our study highlights how spatial working memory is dynamically shaped by experience, underscoring its fundamental role in adaptive foraging and navigation across evolutionary lineages.

Emergence of Structured Navigation is Linked to Spatial Memory Improvements

A fundamental aspect of spatial learning is the progressive refinement of movement patterns, reflecting how animals optimize their navigation strategies over time. Our findings reveal that

as marmosets improved in task performance, their navigation became increasingly structured, transitioning from an initial phase of broad exploration to more consistent and selective transition patterns. This transformation was captured through complementary analyses, including entropy measures and transition matrices, which together provide a comprehensive picture of how experience dynamically shapes spatial behavior. The decline in global entropy across training sessions reflects a fundamental shift from unpredictable, dispersed transitions between dispensers to more stable and precise movement patterns. Notably, this reduction in entropy was strongly correlated with performance improvements, suggesting that as marmosets refined their spatial routines, they also became more efficient in task execution. The progressive stabilization of transition matrices further supports this interpretation: early in training, movement patterns were highly variable, consistent with an exploratory phase lacking clear consistency. Over time, however, these matrices became increasingly similar across sessions, indicating a consolidation of movement preferences and a reduction in overall transition variability. Crucially, these refinements were not merely a by-product of repetition or exposure but rather an active process of optimizing foraging efficiency. This is reinforced by the observed relationship between decreasing entropy and fewer memory errors: as the marmosets' transitions became more organized, their errors also declined. Hence, spatial learning is not just about pruning inefficient movements; it involves the progressive stabilization of structured movement sequences that enhance task efficiency.

Our study provides the first longitudinal evidence of such structured navigation in freely moving non-human primates. Similar patterns have been documented in rodents [34–36], suggesting a possible evolutionary convergence in experience-driven spatial learning mechanisms. These findings underline a crucial aspect of spatial cognition: learning to navigate extends beyond merely reducing errors, involves the gradual emergence of coherent and efficient movement patterns over time. By capturing these refinements, our study provides new insights into how experience shapes spatial learning, leading to the formation of efficient, reproducible navigational routines.

Local Predictability Supports the Emergence of Route-Based Navigation

Having established that structured navigation aligns with performance gains, we next explored whether marmosets relied on rigidly memorized routes or developed a more flexible spatial representation. Spatial learning can manifest in various ways—from fixed, sequential routes to adaptive representations that enable flexible path selection [7]. Disentangling these possibilities is key to understanding the cognitive processes underpinning spatial memory. To quantify navigation patterns at a local level, we used a Markov chain model, which estimates the probability of moving from one dispenser to another based on sequential dependencies. This approach is particularly suited to detecting route-based behavior, as it captures the statistical structure of transitions rather than relying on isolated observations. Crucially, we restricted our analysis to error-free trials, ensuring the model reflected only transitions contributing to successful task execution rather than sporadic, exploratory behaviors.

Our findings strongly support a route-based navigation strategy. The Markov model achieved ~80% prediction accuracy in predicting local transitions—significantly above random levels—revealing a subset of preferred dispenser-to-dispenser transitions. Over repeated sessions, marmosets increasingly relied on these stable routes instead of continuously creating new paths, underscoring a shift toward habitual, structured navigation. This pattern evolved progressively: in early sessions, transitions were highly variable and unpredictable, consistent with an exploratory learning phase. At this stage, marmosets may have depended on visual landmarks to keep track of visited locations [25]. As training advanced, however, navigation became increasingly stable and predictable and transitioned from initial variability to repetitive, efficient route patterns. These observations suggest the reinforcement of successful foraging strategies, in which certain paths are repeated and thus reinforced over time.

Such route-based navigation is reminiscent of behavior in wild marmosets, which systematically reuse specific travel paths to reach feeding and resting sites [21]. Similar behaviors have been observed in other non-human primates (reviewed in [14]), underscoring that repeated experience can stabilize foraging routes even in species known to leverage external cues. By providing longitudinal evidence for the gradual emergence of route-based strategies in a freely moving NHP, our study demonstrates that this navigation pattern is not innate but instead acquired through repeated, self-guided learning experiences.

However, despite the Markov model's ~80% accuracy, it did not capture all aspects of behavior, suggesting that while route-based patterns predominate, some transitions remain unpredictable; particularly at dispensers showing higher local entropy. This indicates that marmosets do not rigidly adhere to a single sequence in every trial. Accordingly, we next turned to a global analysis of full movement sequences to determine whether one route dominates across error-free trials, or several viable routes coexist within their overall navigational repertoire.

Global Flexibility Suggests a Topological Representation

While the Markov model effectively predicted local transitions with high accuracy, its performance declined when applied to full sequences, indicating that although local transitions were highly structured, marmosets did not adhere to a single, rigid path from start to finish. Instead, their navigation exhibited flexibility, allowing variations in sequence execution while still relying on a structured set of transitions. For instance, a dominant sequence often appeared in successful trials, yet the presence of multiple viable sequences implies that animals were not constrained to one solution. Further analysis of sequence variability supports this view. While a dominant sequence appeared in most successful trials, alternative sequences also occurred, demonstrating that marmosets did not rigidly follow a single path. At the same time, a substantial proportion of transitions were consistently reused, suggesting a stable underlying framework guiding navigation. Sequence similarity analyses confirm that numerous sequences shared common transitions, reinforcing the idea that marmosets lean on a core set of preferred transitions while retaining flexibility in path selection. This observation aligns with local entropy results, which showed that although overall local entropy decreased as transitions became more structured, some dispensers retained higher entropy—likely functioning as flexible decision points.

Altogether, this balance between structure and variability suggests a navigation strategy not dependent solely on a predetermined sequence, but rather permitting recombination of transitions. Such findings are consistent with a topological representation of space [7,8], in which marmosets gradually develop an internal cognitive map where locations are connected by multiple potential paths. This conclusion is further supported by observations in wild marmosets, which integrate habitual route segments with flexible decision points[21]. Consequently, in the later training stages, marmosets' navigation is likely guided by a topological map that emerges from experience, enabling them to balance stability and flexibility in complex environments. Thus, rather than following a single rigid route, marmosets displayed a topological flexibility that allowed them to recombine transitions as needed, prompting us to investigate whether the emergence of a dominant sequence– and the eventual resurgence of sequence variability – reflect a broader exploration–exploitation dynamic.

Dynamics of Sequence Use and the Exploration–Exploitation Trade-off

The temporal evolution of sequence predictability provides a deeper look at how marmosets' navigation strategies evolved over the course of training. In early phases, sequences were highly diverse and shared few common transitions, reflecting an exploratory period during which marmosets tested various paths. Correspondingly, a high new-sequence ratio and the

Markov model's difficulty in predicting full sequences corroborate this broad initial exploration. As training progressed, a dominant sequence emerged, accompanied by reduced overall diversity, increased sequence similarity, and a peak in the reused-sequence ratio. At this point, the Markov model achieved high accuracy in predicting entire sequences, indicating that marmosets had converged on a stable, route-based strategy. However, in later stages, sequence diversity rose again while the reused-sequence ratio declined, yet without reverting to full exploration; the new-sequence ratio stayed low, and sequence similarity remained substantial. This pattern suggests that marmosets introduced a degree of flexibility into an otherwise stable network of transitions. Indeed, although the Markov model was less effective at predicting complete sequences during this phase, it continued to excel at local transitions, reinforcing the idea that some adjustments occurred within a topological framework.

Taken together, these observations strongly support the notion of a dynamic balance between stability and variability in navigation. This pattern maps well onto a U-shaped learning trajectory frequently attributed to exploration–exploitation trade-offs [37–39]. Early in learning, individuals explore broadly, leading to high behavioral variability. As effective strategies emerge, variability declines as the system converges on a stable, efficient pattern. Once proficiency is reached, a degree of flexibility can be reintroduced to fine-tune performance and adapt to subtle environmental shifts.

In our study, no external factors were identified that might drive these fluctuations, suggesting that the observed exploration–exploitation dynamic results primarily from internal learning processes. Crucially, the longitudinal nature of our paradigm allowed us to capture the entire progression—from an unstructured phase, to route-based structuring, and ultimately to topological flexibility—a trajectory that would likely remain hidden in shorter or single-phase studies. To our knowledge, this is the first demonstration of such a progressive and adaptable navigation process in freely moving non-human primates.

The behavioral adaptations we observed likely reflect underlying neural processes. While our study does not provide direct neurophysiological evidence, previous research suggests that these patterns may emerge from the dynamic interplay of multiple brain structures

Neural Correlates of Structured and Flexible Navigation

Traditionally, the hippocampus and striatum have been attributed distinct roles in navigation, with the hippocampus supporting cognitive map-based navigation, enabling flexible route planning [5,8], and the striatum facilitating habitual, route-based navigation, where movements become progressively automatized through reinforcement learning [40,41]. However, growing evidence suggests a more integrative model, in which these systems operate in parallel and interact dynamically throughout learning, rather than functioning as independent or competing pathways [42–44].The structured yet flexible navigation patterns observed in our study suggest that hippocampal-striatal interactions may support navigation by integrating learned spatial information with evolving movement strategies, rather than following a strict shift from one system to another.This perspective aligns with evidence that place cells encode more than just metric information; they can also represent spatial relationships in a topological manner, structuring locations as interconnected nodes within a relational graph [45–48]. Moreover, even as navigational behavior becomes more predictable, hippocampal place cells continue to encode behaviorally relevant locations, suggesting that the hippocampus dynamically integrates experience-dependent information rather than simply constructing a static spatial map [34].

Given our observations of structured yet flexible navigation, it is possible that marmosets rely on similar neural mechanisms, where hippocampal and striatal circuits interact to encode key locations, transitions, and learned sequences in a way that supports both flexible navigation

and the refinement of route structures, rather than adhering to a strict dichotomy between map-based and route-based strategies.Notably, place cells have been identified in marmosets [22,23]. Future neurophysiological studies could investigate whether place cell dynamics evolve across training, reflecting the interplay between exploratory behavior and emerging route structures, while striatal activity could reveal its role in optimizing movement sequences without rigid automation.

Beyond these regions, additional circuits likely contribute to navigation flexibility and efficiency. The prefrontal cortex, involved in balancing exploration and exploitation[49], may play a role in strategy refinement, while the posterior parietal cortex, which integrates spatial and motor information[50], could facilitate trajectory selection and movement optimization. Given that marmosets develop structured yet flexible navigation strategies, it is likely that these brain regions interact with hippocampal-striatal circuits to support adaptive spatial behavior.

Taken together, our findings suggest that marmoset navigation arises from a dynamic balance between hippocampal and striatal contributions, potentially supplemented by prefrontal and parietal influences. The semi-naturalistic, unconstrained nature of our task provides an ideal framework to investigate how these neural circuits cooperate to shape spatial learning and decision-making in freely moving primates. Future neurophysiological studies using this paradigm could disentangle the relative contributions of these structures, offering new insights into the neural mechanisms underlying the development, adaptation, and evolution of navigation strategies in non-human primates.

Limitations

While our study provides valuable insights into spatial learning in marmosets, several limitations should be acknowledged. A key constraint is the small sample size, as our findings are based on only two animals. However, this limitation is mitigated by several factors. First, the longitudinal nature of our study allowed us to track individual learning trajectories over extended periods, generating rich within-subject data. Second, behavioral patterns were highly consistent across both animals, suggesting that our results are unlikely to be driven by individual variability. Expanding the sample size in future work will further clarify the generalizability of our findings.

Another challenge in interpreting our results concerns the sensory cues used to guide navigation. Our semi-naturalistic setup is a strength, as it allows animals to express rich, ecologically valid behaviors while spontaneously developing navigation strategies. However, it does not allow for precise control over which sensory cues (e.g., visual landmarks, olfactory cues, proprioceptive feedback) contribute to memory-guided navigation. Future studies could address this by systematically manipulating sensory cues or introducing dynamic spatial changes to determine how different modalities contribute to navigation.

Despite these considerations, our findings provide strong evidence for experience-driven spatial learning in freely moving primates. By capturing the full progression from initial exploration to the formation of structured navigation strategies, our study underscores the importance of longitudinal designs in understanding the learning mechanisms underlying spatial cognition.

Concluding Remarks

By leveraging an unconstrained, ethologically relevant paradigm, our study provides a unique framework for examining the emergence of spatial memory and navigation strategies in primates. Our findings demonstrate that marmosets develop structured yet flexible navigation through experience, reinforcing the idea that spatial learning is a dynamic, adaptive process

rather than a rigid, innate ability. Importantly, our study reproduces natural foraging behaviors observed in wild marmosets, which exhibit route-based navigation while maintaining flexibility in path selection [21]. However, previous field studies could not determine how these strategies emerge due to the lack of experimental control. By replicating these behaviors in a laboratory setting, we show that naturalistic navigation patterns can develop under controlled conditions, allowing for precise investigation of the cognitive mechanisms underlying spatial learning. This highlights the value of neuroethological experimental designs, which enable researchers to systematically manipulate environmental factors while preserving ecological validity. Our study represents a critical first step toward understanding the neural bases of spatial cognition in freely moving non-human primates, providing a behavioral framework to investigate how navigation strategies emerge and evolve through experience. Future studies incorporating neurophysiological recordings will be essential to uncover how multiple brain regions interact dynamically to support adaptive navigation, bridging the gap between naturalistic behavior and its neural underpinnings.

Resource availability

All data and materials used in this study are available upon request to Jean Laurens. Custom scripts for data analysis can be provided upon request to Nada El Mahmoudi.

Acknowledgments

We thank the animal care staff at the Ernst Strüngmann Institute for their assistance in ensuring the welfare of the marmosets. This work was supported by Bundesministerium für Bildung und Forschung (ERANET NEURON 01EW2110).

Author contributions

Nada El Mahmoudi: Conceptualization, Methodology, Data Collection, Formal Analysis, Writing – Original Draft, Writing – Review & Editing
Francesca Lanzarini: Conceptualization, Methodology, Data Collection, Writing – Original Draft, Writing – Review & Editing
Farzad Ziaie Nezhad: Technical Support, Writing – Review & Editing
Deepak Surendran: Technical Support, Writing – Review & Editing
Jean Laurens: Supervision, Funding Acquisition, Conceptualization, Writing – Review & Editing

All authors read and approved the final manuscript.

Declaration of interests

The authors declare no competing financial or non-financial interests related to this work.

References

1. Olton, D.S. (1977). Spatial Memory. Scientific American *236*, 82–99.
2. Olton, D.S., Becker, J.T., and Handelmann, G.E. (1979). Hippocampus, space, and memory. Behav Brain Sci *2*, 313–322. https://doi.org/10.1017/S0140525X00062713.

3. Arleo, A., and Rondi-Reig, L. (2007). Multimodal sensory integration and concurrent navigation strategies for spatial cognition in real and artificial organisms. J. Integr. Neurosci. *06*, 327–366. https://doi.org/10.1142/S0219635207001593.
4. Burgess, N. (2006). Spatial memory: how egocentric and allocentric combine. Trends in Cognitive Sciences *10*, 551–557. https://doi.org/10.1016/j.tics.2006.10.005.
5. O'Keefe, J., and Nadel, L. (1978). The hippocampus as a cognitive map (Clarendon Press ; Oxford University Press).
6. Redish, A.D. (1999). Beyond the Cognitive Map: From Place Cells to Episodic Memory (A Bradford Book).
7. Parra-Barrero, E., Vijayabaskaran, S., Seabrook, E., Wiskott, L., and Cheng, S. (2023). A map of spatial navigation for neuroscience. Neuroscience & Biobehavioral Reviews *152*, 105200. https://doi.org/10.1016/j.neubiorev.2023.105200.
8. Poucet, B. (1993). Spatial cognitive maps in animals: New Hypotheses on their structure and neural mechanisms. Psychological review *100*, 163–182. https://doi.org/10.1037/0033-295X.100.2.163.
9. Geva-Sagiv, M., Las, L., Yovel, Y., and Ulanovsky, N. (2015). Spatial cognition in bats and rats: from sensory acquisition to multiscale maps and navigation. Nat Rev Neurosci *16*, 94–108. https://doi.org/10.1038/nrn3888.
10. Morris, R.G.M., Garrud, P., Rawlins, J.N.P., and O'Keefe, J. (1982). Place navigation impaired in rats with hippocampal lesions. Nature *297*, 681–683. https://doi.org/10.1038/297681a0.
11. Sutherland, R.J., and Hamilton, D.A. (2004). Rodent spatial navigation: at the crossroads of cognition and movement. Neuroscience & Biobehavioral Reviews *28*, 687–697. https://doi.org/10.1016/j.neubiorev.2004.09.012.
12. Tolman, E.C. (1948). Cognitive maps in rats and men. Psychological Review *55*, 189–208. https://doi.org/10.1037/h0061626.
13. Wang, C., Chen, X., and Knierim, J.J. (2020). Egocentric and allocentric representations of space in the rodent brain. Current Opinion in Neurobiology *60*, 12–20. https://doi.org/10.1016/j.conb.2019.11.005.
14. Trapanese, C., Meunier, H., and Masi, S. (2019). What, where and when: spatial foraging decisions in primates. Biological Reviews *94*, 483–502. https://doi.org/10.1111/brv.12462.
15. Mao, D. (2022). Neural Correlates of Spatial Navigation in Primate Hippocampus. Neurosci Bull *39*, 315–327. https://doi.org/10.1007/s12264-022-00968-w.
16. Abreu, F., De la Fuente, M.F.C., Schiel, N., and Souto, A. (2016). Feeding ecology and behavioral adjustments: flexibility of a small neotropical primate (Callithrix jacchus) to survive in a semiarid environment. Mamm Res *61*, 221–229. https://doi.org/10.1007/s13364-016-0262-4.
17. Garber, P.A. (1992). Vertical clinging, small body size, and the evolution of feeding adaptations in the Callitrichinae. American Journal of Physical Anthropology *88*, 469–482. https://doi.org/10.1002/ajpa.1330880404.
18. Schiel, N., and Souto, A. (2017). The common marmoset: An overview of its natural history, ecology and behavior. Developmental Neurobiology *77*, 244–262. https://doi.org/10.1002/dneu.22458.
19. Xavier, D.P., Abreu, F., Souto, A., and Schiel, N. (2024). Choosing the best way: how wild common marmosets travel to efficiently exploit resources. Anim Cogn *27*, 20. https://doi.org/10.1007/s10071-024-01864-8.
20. Abreu, F., Souto, A., and Schiel, N. (2020). Wild common marmosets (Callithrix jacchus) employ spatial cognitive abilities to improve their food search and consumption: an experimental approach in small-scale space. Primates *61*, 807–816. https://doi.org/10.1007/s10329-020-00826-1.
21. Abreu, F., Garber, P.A., Souto, A., Presotto, A., and Schiel, N. (2021). Navigating in a challenging semiarid environment: the use of a route-based mental map by a small-bodied neotropical primate. Anim Cogn *24*, 629–643. https://doi.org/10.1007/s10071-020-01465-1.

22. Courellis, H.S., Nummela, S.U., Metke, M., Diehl, G.W., Bussell, R., Cauwenberghs, G., and Miller, C.T. (2019). Spatial encoding in primate hippocampus during free navigation. PLOS Biology *17*, e3000546. https://doi.org/10.1371/journal.pbio.3000546.
23. Piza, D.B., Corrigan, B.W., Gulli, R.A., Do Carmo, S., Cuello, A.C., Muller, L., and Martinez-Trujillo, J. (2024). Primacy of vision shapes behavioral strategies and neural substrates of spatial navigation in marmoset hippocampus. Nat Commun *15*, 4053. https://doi.org/10.1038/s41467-024-48374-2.
24. MacDonald, S.E., Pang, J.C., and Gibeault, S. (1994). Marmoset (Callithrix jacchus jacchus) spatial memory in a foraging task: Win-stay versus win-shift strategies. Journal of Comparative Psychology *108*, 328–334. https://doi.org/10.1037/0735-7036.108.4.328.
25. MacDonald, S.E., Spetch, M.L., Kelly, D.M., and Cheng, K. (2004). Strategies in landmark use by children, adults, and marmoset monkeys. Learning and Motivation *35*, 322–347. https://doi.org/10.1016/j.lmot.2004.03.002.
26. Dudchenko, P.A. (2004). An overview of the tasks used to test working memory in rodents. Neuroscience & Biobehavioral Reviews *28*, 699–709. https://doi.org/10.1016/j.neubiorev.2004.09.002.
27. Olton, D.S., and Samuelson, R.J. (1976). Remembrance of places passed: Spatial memory in rats. Journal of Experimental Psychology: Animal Behavior Processes *2*, 97–116. https://doi.org/10.1037/0097-7403.2.2.97.
28. Dennis, E.J., Hady, A.E., Michaiel, A., Clemens, A., Tervo, D.R.G., Voigts, J., and Datta, S.R. (2021). Systems Neuroscience of Natural Behaviors in Rodents. J. Neurosci. *41*, 911–919. https://doi.org/10.1523/JNEUROSCI.1877-20.2020.
29. Lanzarini, F., Maranesi, M., Rondoni, E.H., Albertini, D., Ferretti, E., Lanzilotto, M., Micera, S., Mazzoni, A., and Bonini, L. (2025). Neuroethology of natural actions in freely moving monkeys. Science *387*, 214–220. https://doi.org/10.1126/science.adq6510.
30. Miller, C.T., Gire, D., Hoke, K., Huk, A.C., Kelley, D., Leopold, D.A., Smear, M.C., Theunissen, F., Yartsev, M., and Niell, C.M. (2022). Natural behavior is the language of the brain. Current Biology *32*, R482–R493. https://doi.org/10.1016/j.cub.2022.03.031.
31. Nakamura, K., Koba, R., Miwa, M., Yamaguchi, C., Suzuki, H., and Takemoto, A. (2018). A Method to Train Marmosets in Visual Working Memory Task and Their Performance. Front. Behav. Neurosci. *12*. https://doi.org/10.3389/fnbeh.2018.00046.
32. El Mahmoudi, N., Laurent, C., Péricat, D., Watabe, I., Lapotre, A., Jacob, P.-Y., Tonetto, A., Tighilet, B., and Sargolini, F. (2023). Long-lasting spatial memory deficits and impaired hippocampal plasticity following unilateral vestibular loss. Progress in Neurobiology *223*, 102403. https://doi.org/10.1016/j.pneurobio.2023.102403.
33. Roberts, W.A., Macpherson, K., Robinson, S., Hennessy, A., and Richmond, B. (2024). Rat spatial memory and foraging on dual radial mazes. Learn Behav *52*, 51–59. https://doi.org/10.3758/s13420-023-00592-2.
34. Dupret, D., O'Neill, J., Pleydell-Bouverie, B., and Csicsvari, J. (2010). The reorganization and reactivation of hippocampal maps predict spatial memory performance. Nat Neurosci *13*, 995–1002. https://doi.org/10.1038/nn.2599.
35. Wathen, C.N., and Roberts, W.A. (1994). Multiple-pattern learning by rats on an eight-arm radial maze. Animal Learning & Behavior *22*, 155–164. https://doi.org/10.3758/BF03199915.
36. Yoerg, S.I., and Kamil, A.C. (1982). Response strategies in the radial arm maze: Running around in circles. Animal Learning & Behavior *10*, 530–534. https://doi.org/10.3758/BF03212295.
37. Cohen, J.D., McClure, S.M., and Yu, A.J. (2007). Should I stay or should I go? How the human brain manages the trade-off between exploitation and exploration. Philosophical Transactions of the Royal Society B: Biological Sciences *362*, 933–942. https://doi.org/10.1098/rstb.2007.2098.
38. Mehlhorn, K., Newell, B.R., Todd, P.M., Lee, M.D., Morgan, K., Braithwaite, V.A., Hausmann, D., Fiedler, K., and Gonzalez, C. (2015). Unpacking the exploration–exploitation tradeoff: A synthesis of human and animal literatures. Decision *2*, 191–215. https://doi.org/10.1037/dec0000033.

39. Sutton, R.S., and Barto, A.G. (1998). Reinforcement Learning: An Introduction (The MIT Press).
40. Meer, M.A.A. van der, Johnson, A., Schmitzer-Torbert, N.C., and Redish, A.D. (2010). Triple Dissociation of Information Processing in Dorsal Striatum, Ventral Striatum, and Hippocampus on a Learned Spatial Decision Task. Neuron *67*, 25–32. https://doi.org/10.1016/j.neuron.2010.06.023.
41. Packard, M.G., and McGaugh, J.L. (1996). Inactivation of Hippocampus or Caudate Nucleus with Lidocaine Differentially Affects Expression of Place and Response Learning. Neurobiology of Learning and Memory *65*, 65–72. https://doi.org/10.1006/nlme.1996.0007.
42. Brown, T.I., Ross, R.S., Tobyne, S.M., and Stern, C.E. (2012). Cooperative interactions between hippocampal and striatal systems support flexible navigation. NeuroImage *60*, 1316–1330. https://doi.org/10.1016/j.neuroimage.2012.01.046.
43. Goodman, J. (2021). Place vs. Response Learning: History, Controversy, and Neurobiology. Front. Behav. Neurosci. *14*. https://doi.org/10.3389/fnbeh.2020.598570.
44. Goodroe, S.C., Starnes, J., and Brown, T.I. (2018). The Complex Nature of Hippocampal-Striatal Interactions in Spatial Navigation. Front. Hum. Neurosci. *12*. https://doi.org/10.3389/fnhum.2018.00250.
45. Alvernhe, A., Cauter, T.V., Save, E., and Poucet, B. (2008). Different CA1 and CA3 Representations of Novel Routes in a Shortcut Situation. J. Neurosci. *28*, 7324–7333. https://doi.org/10.1523/JNEUROSCI.1909-08.2008.
46. Babichev, A., Cheng, S., and Dabaghian, Y.A. (2016). Topological Schemas of Cognitive Maps and Spatial Learning. Front. Comput. Neurosci. *10*. https://doi.org/10.3389/fncom.2016.00018.
47. Chen, Z., Gomperts, S.N., Yamamoto, J., and Wilson, M.A. (2014). Neural representation of spatial topology in the rodent hippocampus. Neural Comput *26*, 1–39. https://doi.org/10.1162/NECO_a_00538.
48. Dabaghian, Y., Brandt, V.L., and Frank, L.M. (2014). Reconceiving the hippocampal map as a topological template. eLife *3*, e03476. https://doi.org/10.7554/eLife.03476.
49. Daw, N.D., O'Doherty, J.P., Dayan, P., Seymour, B., and Dolan, R.J. (2006). Cortical substrates for exploratory decisions in humans. Nature *441*, 876–879. https://doi.org/10.1038/nature04766.
50. Whitlock, J.R., Sutherland, R.J., Witter, M.P., Moser, M.-B., and Moser, E.I. (2008). Navigating from hippocampus to parietal cortex. Proceedings of the National Academy of Sciences *105*, 14755–14762. https://doi.org/10.1073/pnas.0804216105.
51. Buffalo, E.A., Movshon, J.A., and Wurtz, R.H. (2019). From basic brain research to treating human brain disorders. Proceedings of the National Academy of Sciences *116*, 26167–26172. https://doi.org/10.1073/pnas.1919895116.
52. Ludvig, N., Tang, H.M., Eichenbaum, H., and Gohil, B.C. (2003). Spatial memory performance of freely-moving squirrel monkeys. Behavioural Brain Research *140*, 175–183. https://doi.org/10.1016/S0166-4328(02)00325-X.
53. Laurens, J. (2022). The statistical power of three monkeys. Preprint at bioRxiv, https://doi.org/10.1101/2022.05.10.491373 https://doi.org/10.1101/2022.05.10.491373.
54. Friard, O., and Gamba, M. (2016). BORIS: a free, versatile open-source event-logging software for video/audio coding and live observations. Methods in Ecology and Evolution *7*, 1325–1330. https://doi.org/10.1111/2041-210X.12584.

Methods

1. Ethical Statement

All animal procedures in this study were approved by the relevant regional government authority (F149/1012) and adhered to all applicable German and European regulations on animal husbandry and welfare. A small-sample approach was adopted, in line with previous research on spatial behavior in freely moving non-human primates [24,25,51,52].This approach

allowed for a substantial amount of data to be collected per animal, minimizing the need for a larger sample while maintaining methodological rigor[53].

2. Animals and Housing

Two adult male common marmosets (*Callithrix jacchus*; mean age: 3 years) participated in this study. The animals were pair-housed in a cage measuring 180 cm (H) × 90 cm (W) × 60 cm (D) under a 12-hour light-dark cycle (07:00–19:00). Room temperature was maintained at 24–25°C with 60% relative humidity. The marmosets were obtained from the German Primate Center (Göttingen, Germany). Experimental sessions took place in the morning. In addition to the gum arabic collected during the task, animals were fed a daily meal consisting of pellets; a dietary supplement primarily composed of quark, yogurt, banana and vitamins; and fresh vegetables. Water was provided ad libitum.

3. Experimental Apparatus and Data Collection

The experimental setup consisted of a wire mesh enclosure measuring 1.8 m × 1.4 m × 1.6 m (total volume: 4 cubic meters). The wire mesh walls facilitated climbing and allowed the marmosets to navigate freely within the space. The entrance was located in a designated corner, where a tunnel system enabled transition from the transport cage to the setup. To encourage locomotion and exploratory behavior, the enclosure was enriched with wooden sticks, semi-rigid ropes, and suspended enrichment items (**Fig.1A**). Additional environmental cues were introduced around the enclosure, including four white walls with landscape posters, four colored curtains, and large plastic plants.

During each experimental session, rewards were dispensed using custom-made, 3D-printed, remotely controlled dispensers (**Fig. 1A, E**). Each dispenser was calibrated to deliver 3 ml of liquid gum arabic per session, in increments of approximately 0.15 ml per activation. To ensure accurate dispensing, the system was tested and calibrated prior to each session.

Two experimenters conducted the sessions individually, alternating roles between sessions. During each session, the experimenter was positioned at a fixed location at a predetermined distance from the setup, manually scoring dispenser visits and task latencies in real time using BORIS, a well-established behavioral event logging software [54]. A visit to a dispenser was defined as the marmoset pausing in front of the dispenser and attempting to retrieve the reward. This criterion ensured that only purposeful interactions with the dispenser were recorded as visits. Additionally, a wide-angle lens camera was mounted above the setup, continuously recording the sessions for further analysis.

4. Behavioral Training

4.1 Habituation

Before the experiment, the marmosets underwent a habituation phase to ensure they did not exhibit anxiety and displayed natural exploratory behavior in the setup. This process took place over multiple sessions and was conducted by both experimenters, who had prior experience training the animals. As a result, the marmosets were well-acquainted with both experimenters before the start of behavioral testing. Initially, the two marmosets were trained to be comfortably transported from the animal facility to the laboratory in a transport cage. They were then introduced together into the setup, where they could explore and discover hidden rewards (e.g., marshmallows) placed in various locations. In the final habituation phase, only one marmoset entered the setup at a time, while the second remained in the transport cage nearby, maintaining visual contact. Initially, the separation lasted only a few minutes but gradually increased until the marmoset could remain alone for at least 30 minutes without signs of

discomfort. Throughout this process, the experimenter monitored welfare by assessing vocalizations and behaviors based on established ethological criteria for captive marmosets [18].

4.2 Home Dispenser Training

Since the marmosets explored the setup freely, they needed to be trained to voluntarily move to the center of the apparatus when required, ensuring that each trial started from a standardized position during the spatial working memory task. To achieve this, a food dispenser (i.e the “Home Dispenser (HD)”) was installed upside down at the center of the ceiling (**Fig.1E**). The HD contained liquid gum arabic and was equipped with a blue LED and a buzzer, providing visual and auditory cues upon activation. Using positive reinforcement, the monkeys were trained to associate these cues with the HD activation and to reach it promptly.

Each marmoset was tested individually. At the start of each trial, the HD was activated for ~3 seconds, signaling the monkey to move to the center. The subject had up to 60 seconds to reach the HD for the trial to be considered successful. If the monkey failed to do so within this timeframe, the trial was marked as unsuccessful. A session was terminated if the monkey failed to complete two consecutive trials. Performance was evaluated based on the number of successful trials per session and the latency to reach the HD. Training was considered complete once the monkey achieved over 80% successful trials in two consecutive sessions. On average, each session consisted of 20.4 ± 1.19 trials for Animal E and 16.05 ± 1.2 trials for Animal F. To reach the training completion criterion, Animal E required 10 sessions, while Animal F needed 18 sessions.

5. Spatial working memory task (Behavioral testing)

The experiment assessed spatial working memory by requiring marmosets to retrieve rewards from eight dispensers while remembering which ones they had already visited.

During the testing phase, eight additional dispensers were introduced, placed in fixed locations along the perimeter of the setup to ensure uniform spatial coverage (**Fig.1A**). Specifically, three dispensers were placed equidistantly along each of the two long sides, while one dispenser was positioned at the midpoint of each short side. This configuration ensured consistent spatial cues and a uniform distribution of reward locations across trials.

At the start of each trial, the Home Dispenser (HD) was activated, prompting the monkey to move to the center of the apparatus within 60 seconds. Once the monkey reached the HD, all eight dispensers were remotely activated simultaneously (**Fig.1B**)., each releasing ~0.15 ml of gum arabic as a reward. The food was concealed within the spout of each dispenser and not visible to the monkey, requiring them to actively search for and retrieve it. The reward remained available until collected.

To successfully complete the trial, the monkey had to visit all eight dispensers at least once, retrieving the reward from each. The trial ended upon the first visit to the eighth unique dispenser, regardless of whether the monkey revisited some dispensers along the way. However, if the monkey failed to visit all eight dispensers within 10 minutes, the trial was automatically terminated. After trial completion or timeout, the HD was reactivated, signaling the start of the next trial.

Each monkey underwent 30 training sessions, with an average of 7.96±0.4 trials for Animal E and 8±0.4 trials for Animal F per session. A session was terminated if the monkey failed to complete two consecutive trials.

6. Data analysis

All data analyses were performed in Python using custom-made scripts and libraries such as numpy, pandas, statsmodels, scipy, scikit-posthocs, seaborn, and plotly for statistical analysis and visualization. Given the single-subject design, non-parametric tests were preferred. When needed, parametric analyses were conducted with model assumptions systematically verified, and robust standard errors applied when necessary. Bonferroni corrections were used to control for multiple comparisons. Statistical significance was set at $\alpha = 0.05$, with additional thresholds reported for $p < 0.01$ and $p < 0.001$ where relevant.

6.1 Spatial distribution of visits and omissions

To assess whether the marmosets interacted equally with all dispensers, we analyzed the number of visits and omissions for each of the eight dispensers. We first used Chi-squared tests to compare the observed visit and omission distributions to an expected uniform distribution, testing whether interaction patterns were evenly distributed. If a significant deviation was detected, binomial tests were conducted for each dispenser to identify which ones had visit frequencies that significantly differed from chance. A Bonferroni correction was applied to control for multiple comparisons.

6.2. Error Analysis and Regression Across Sessions

To assess error patterns across training sessions, errors were categorized into three types: rule errors (returning to the home dispenser during a trial), repetition errors (revisiting a dispenser within the same trial), and omission errors (failing to visit a dispenser). The total number of errors per trial was computed and averaged per session to obtain the mean number of errors per session and the standard error of the mean (SEM).

A linear regression analysis was performed to evaluate changes in the mean number of errors over time, with session number as the independent variable. The slope of the regression line was examined to determine whether errors decreased with training. Model fit was assessed using R-squared values, and confidence intervals were computed to visualize prediction uncertainty. To ensure the validity of the regression model, key assumptions were tested: normality of residuals was assessed using the Omnibus test, independence of errors was verified with the Durbin-Watson statistic, and homoscedasticity was examined using the Breusch-Pagan test. Heteroscedasticity, if detected, was addressed by computing robust standard errors.

To further investigate factors influencing error rates, a multiple linear regression was conducted with session number, number of trials, number of days since the last session, and experimenter identity as independent variables. Model assumptions were systematically tested to ensure the validity of the regression analysis. Normality of residuals was assessed using the Shapiro-Wilk test, homoscedasticity was evaluated with the Levene test, and multicollinearity was examined through the Variance Inflation Factor (VIF). Ordinary Least Squares (OLS) regression with heteroscedasticity-robust standard errors was applied to account for variance inconsistencies. To control for multiple comparisons, p-values were adjusted using Bonferroni corrections.

6.3 Error Type Dynamics and Correlation Analysis

To examine the evolution of error types across training, we calculated the mean number and SEM of rule errors, repetition errors, and omission errors per session. A Kruskal-Wallis test

was used to assess whether these error distributions differed significantly across sessions, followed by Dunn's post hoc test with Bonferroni correction for multiple comparisons. To explore relationships between error types, two correlation matrices were computed: one at the session level, where values were averaged per session, and one at the trial level, using individual trial data. Both matrices included total errors, total number of visits, rule errors, repetition errors, and omission errors. Pearson's correlation coefficients were used to assess linear associations, with Bonferroni correction applied to control for multiple comparisons.

6.4. Clustering analysis

6.4.1 Clustering procedure

We conducted a K-Means clustering analysis to identify distinct behavioral patterns in marmoset task execution based on omission errors (failing to visit a dispenser) and total visits to dispensers. These two variables were selected to capture complementary aspects of task engagement, with omission errors reflecting disengagement and total visits indicating active task participation. Prior to clustering, the data were standardized to ensure equal weighting of both variables. The optimal number of clusters was determined by balancing silhouette scores and inertia, which assess cluster separation and within-cluster cohesion, respectively. Each trial was then assigned to a cluster based on proximity to the cluster centroids, representing the mean omission errors and total visits per cluster.

6.4.2 Statistical Comparison Between Clusters

To assess differences in task performance among the clusters identified by K-Means clustering, we analyzed several performance variables, including trial duration, total number of visits, and error types (rule errors, repetition errors, and omission errors). A Kruskal-Wallis test was conducted to determine whether these variables differed significantly across clusters. If significant differences were detected ($p < 0.05$), Dunn's post-hoc test was performed for pairwise comparisons, with a Bonferroni correction applied to control for multiple comparisons.

6.4.3 Regression Analysis of Cluster Proportions Across Sessions

A linear regression analysis was performed to evaluate changes in the proportion of trials assigned to each cluster over training, with session number as the independent variable. Separate ordinary least squares (OLS) regression models were fitted for each cluster. The slope of the regression line was examined to determine whether the proportion of trials in each cluster changed significantly over time. Model fit was assessed using R-squared values, and confidence intervals were computed to visualize prediction uncertainty. To ensure the validity of the regression models, normality of residuals was assessed, independence of errors was verified using the Durbin-Watson statistic, and homoscedasticity was examined using the Breusch-Pagan test. When necessary, heteroscedasticity was addressed by computing robust standard errors.

6.5 Analysis of performance over the first eight choices

To assess task performance, we analyzed the success rate over the first eight choices, defined as the proportion of correct responses within these first eight selections. A response was considered correct if the marmoset selected a dispenser that had not been visited previously in the trial. This analysis was performed in two contexts: (1) comparison between clusters 0 and 1, and (2) evolution of performance across training phases.

6.5.1 Cluster Performance Analysis

To determine whether performance within each cluster differed from what would be expected under random selection, we computed the expected random performance assuming choices were made randomly among nine available options. Since the number of remaining correct options decreases at each step, the probability of selecting a correct option follows this sequence:

Equation 1:

$$P_{\text{random}} = \frac{8}{9} \times \frac{7}{9} \times \frac{6}{9} \times \frac{5}{9} \times \frac{4}{9} \times \frac{3}{9} \times \frac{2}{9} \times \frac{1}{9}$$

The expected average success rate was then computed as:

Equation 2:

$$E\left(\text{performance}_{\text{random}}\right) = \frac{1}{8} \sum_{i=1}^{8} \frac{9-i}{9} = 0.5$$

Thus, under random selection, the expected success rate is 50%, meaning that, on average, a marmoset would make 4 correct choices out of 8 by chance. This value served as a baseline for evaluating observed performance in each cluster.

For each cluster, we calculated the mean success rate and SEM. To assess whether cluster performance significantly deviated from the random expectation, we performed a Wilcoxon signed-rank test against the 50% baseline, with Bonferroni correction applied for multiple comparisons. Pairwise comparisons between clusters were conducted using a Mann-Whitney U test.

6.5.2 Performance Evolution Across Training Phases

To evaluate changes in performance over training, we divided the training sessions into six phases, each consisting of five sessions: the first ten sessions were divided into Beg 1 (S1–S5) and Beg 2 (S6–S10); the ten intermediate sessions into Int 1 (S11–S15) and Int 2 (S16–S20); and the last ten sessions into Last 1 (S21–S25) and Last 2 (S26–S30). For each phase, we computed the mean performance rate and SEM. Performance rates were compared across these six phases using a Kruskal-Wallis test to determine whether task performance significantly improved over time.

6.6. Transition Patterns Analysis

6.6.1 Cluster Analysis

<u>6.6.1.1 Transition Probability Computation</u>

Each trial was represented as a sequence of visits to dispensers. Transition probabilities between locations were calculated by determining the frequency of transitions from one dispenser to another. The probability of transitioning from dispenser i to dispenser j was defined as:

Equation 3:

$$P(i \to j) = \frac{\text{Number of transitions from } i \text{ to } j}{\sum_k \text{Number of transitions from } i \text{ to } k}$$

Where $P(i \to j)$ is the probability of transitioning from dispenser i to dispenser j, and the denominator is the total number of transitions starting from dispenser i to any possible dispenser (the sum over all possible dispensers k).

To ensure comparability across clusters, we considered all possible transitions—including those with zero occurrences—and then normalized the transition probability matrix on a row-by-row basis. In other words, for each dispenser (row), we scaled the counts so that the sum of the probabilities for all transitions starting from that dispenser equals one.

6.6.1.2 Global Entropy and Global Transition Diversity

For the calculation of global entropy and global transition diversity, the transition probability matrix was further normalized globally. That is, after computing the row-wise transition probabilities for each dispenser, we rescaled the entire matrix so that the sum of all transition probabilities within each cluster equals 1. This global normalization allows for a direct comparison of transition patterns between clusters.

We calculated global entropy based on Shannon entropy's formula:

Equation 4:

$$H = -\sum P(i \to j) \log_2 P\,(i \to j)$$

Where $P(i \to j)$ represents the probability of transitioning from dispenser i to dispenser j. In this context, global entropy quantifies the overall unpredictability of transitions across all dispensers: higher entropy values indicate that transitions are more varied and less predictable, while lower values suggest a more structured, stereotyped pattern dominated by a few transitions.

In addition, we calculated global transition diversity using Simpson's Diversity Index to assess the evenness of transition probabilities between dispensers. The index was computed as:

Equation 5:

$$D = 1 - \sum P(i \to j)^2$$

In the context of transition patterns, global transition diversity represents the overall distribution of transition probabilities across all dispensers. A higher diversity value indicates that transitions are more evenly spread across dispensers, meaning that no single transition overwhelmingly dominates the movement pattern. Conversely, lower diversity suggests that only a few transitions occur more frequently, leading to more repetitive and less varied behavior.

To estimate the variability and compute confidence intervals for global entropy and global transition diversity, we performed a bootstrap resampling procedure with 1,000 iterations. In each iteration, transition probabilities were resampled with replacement, and entropy and

diversity values were recomputed. The 95% confidence intervals (CI) were derived from the 2.5th and 97.5th percentiles of the bootstrap distributions.

6.6.1.3 Simulation of Random Behavior for Baseline Comparison

To establish a baseline for global entropy and global transition diversity under random movement conditions, we simulated random sequences of visits and computed their expected entropy and diversity values. A total of 1,000 simulations were performed, each consisting of 1,000 randomly generated sequences of 8 visits (excluding the starting location). In each sequence, dispensers were selected randomly with replacement, ensuring no systematic preference for specific locations. Transition counts were collected across all simulated sequences to compute empirical random transition probabilities. These probabilities were globally normalized to ensure comparability with the observed data. From these simulations, we calculated the mean global entropy and global transition diversity, and derived confidence intervals (at the 95%, 99%, and 99.9% levels) based on the corresponding percentiles of the bootstrap distributions.

6.6.1.4 Permutation Test for Statistical Comparison

Permutation tests were applied to compare the observed global entropy and global transition diversity of each cluster to both the random baseline and between clusters. In 1,000 iterations, the observed data and simulated baseline were pooled, and data were randomly reassigned to two groups of equal size. The mean difference in global entropy and global transition diversity was calculated for each permutation, generating a null distribution. Bonferroni corrections were applied to adjust for multiple comparisons.

6.6.1.5 Transition Matrices

To investigate the behavioral transition patterns, transition matrices were calculated for each cluster, representing the transition probabilities between dispensers across trials. These matrices were computed for both global transitions (including all observed transitions) and significant transitions (those that were significantly different from random chance).

Transition matrices were constructed by counting the frequency of transitions between dispensers across all trials. Transition probabilities were then normalized so that the sum of probabilities for each row (representing outgoing transitions from a dispenser) equaled 1.

To identify statistically significant transitions, binomial tests were conducted for each transition in the matrix, comparing the observed transition probabilities to a uniform random baseline of 1/9 (assuming each dispenser is equally likely to be chosen). Bonferroni correction was applied to adjust for multiple comparisons. Only transitions with corrected p-values less than 0.05 were considered significant.

The similarity between the transition matrices of different clusters was assessed by computing the correlation between their flattened versions. A permutation test with 1,000 iterations was applied to randomly shuffle the values in each matrix pair and compare the correlation of the shuffled matrices to the observed correlation. This process allowed the calculation of a p-value for the correlation, which quantified the likelihood of obtaining the observed correlation by chance. Additionally, the Euclidean distance between the transition matrices was calculated to measure the dissimilarity between matrices, with smaller distances indicating greater similarity.

6.6.1.6 Transition Probability Mapping

To visualize the structure of movement patterns, transition maps were generated for each cluster based on the first 8 choices of each trial. These patterns were visualized using directed graphs where all transition probabilities were represented by a weighted graph, with edge thickness proportional to the transition probability. Significant transitions were represented as a subset of transitions meeting statistical significance.

6.6.2 Analysis by Training Part

6.6.2.1 Transition Probability Computation

The computation of transition probabilities followed the methodology described in section 6.6.1.1. Briefly, each trial was represented as a sequence of dispenser visits, and transition probabilities were calculated from the frequency of transitions between dispensers. To ensure comparability across training phases, we considered all possible transitions—even those with zero occurrences—and normalized the resulting probabilities on a row-by-row basis (i.e., for each dispenser, the sum of the probabilities of transitions from that dispenser was scaled to equal 1).

6.6.2.2 Global Entropy

Global entropy analysis for training phases was conducted in the same way as in Section 6.6.1.2 section. Transition probabilities were globally normalized, so that the sum of all transition probabilities within each cluster equaled 1 and Shannon entropy was computed to measure the unpredictability of transition patterns within each training phase. Bootstrap resampling with 1,000 iterations was used to estimate the variability of entropy values, as described in 6.6.1.2. The 95% confidence intervals (CI) for entropy were derived from the 2.5th and 97.5th percentiles of the bootstrap distributions. Permutation tests were applied to compare the observed entropy between training phases. In 1,000 iterations, data were pooled and randomly reassigned to two groups. The mean difference in entropy was calculated for each permutation, and Bonferroni corrections were applied to adjust for multiple comparisons.

6.6.2.3 Overlap Index Calculation

To assess the degree of similarity between entropy distributions from different training phases, we calculated the Overlap Index. This index measures the shared area between two probability distributions and provides an indication of how similar the transition behaviors are between phases. The index ranges from 0 to 1, with 0 indicating no similarity and 1 indicating complete similarity in the transition patterns. For each pair of training phases, the entropy distributions were calculated, and histograms were constructed with 100 bins, covering the range of observed entropy values. The Overlap Index was then determined by summing, across all bins, the minimum value between the corresponding bins of the two histograms. Higher Overlap Index values indicate greater similarity in the transition patterns between dispensers across training phases

6.6.2.4 Correlation between global entropy and performance rate

To evaluate the linear relationship between the mean performance rate (across the first 8 choices) and the mean global entropy, their correlation was assessed using Pearson's correlation coefficient across all training phases. Bonferroni correction was applied to account for multiple comparisons. Additionally, a linear regression model was fitted to the data to visually represent and further assess the relationship between these two variables.

6.6.2.5 Transition Matrices

Transition matrices for each training phase were calculated following the same approach as

in the 6.6.1.5 section. Significant transitions were identified using binomial tests, with Bonferroni corrections for multiple comparisons.

6.6.2.6 Transition Probability Mapping

Transition maps were generated for each training phase in the same manner as in Section 6.6.1.6. Significant transitions were identified based on binomial tests, and Bonferroni corrections were applied for multiple comparisons.

6.6.2.7 Local Entropy

Local entropy quantifies the unpredictability of transitions at the individual dispenser level. For each dispenser, we first calculated the transition probabilities, that is, the likelihood of transitioning from that dispenser to each of the other dispensers. The local entropy for a dispenser was then computed using Shannon's entropy formula:

Equation 6:

$$H(X) = -\sum_{i} p(x_i) \log_2 p\,(x_i)$$

Where $p(x_i)$ represents the probability of transitioning to dispenser i. For dispensers with no outgoing transitions, the entropy was set to zero. In this context, higher local entropy values indicate greater variability (i.e., less predictable and more diverse transitions), whereas lower values suggest more structured, predictable transition patterns.

To assess whether local entropy values differed significantly across training phases, we applied the Kruskal–Wallis test. When significant differences were detected, pairwise comparisons were performed using Dunn's post-hoc test with Bonferroni correction.

6.6.2.8 Error Probability

For each dispenser, we calculated error probability as the proportion of errors that occurred following a visit to that dispenser. Specifically, for each training phase, we counted the number of errors that immediately followed visits to each dispenser and divided that number by the total number of trials in that phase. This provided an estimate of the likelihood of making an error after visiting a given dispenser, relative to the overall number of trials—in other words, the probability of an error in any given trial when that dispenser is involved. To assess whether error probabilities differed significantly across training phases, we applied the Kruskal–Wallis test. When significant differences were detected, Dunn's post-hoc test with Bonferroni correction was used to identify which specific phases differed.

6.6.2.9 Correlation between Local Entropy and Error Probability

To evaluate the linear relationship between mean local entropy and mean error probability, Pearson's correlation coefficient was computed using data from all training phases combined. A Bonferroni correction was applied to adjust for multiple comparisons. Additionally, a linear regression model was fitted to the data to visually represent and further assess the relationship between these two variables.

6.7. Markov Model Analysis

The Markov model was trained exclusively on error-free trials to focus on transition patterns observed during successful task performance. This section describes the methods used to construct the transition matrix, predict transitions, evaluate performance, and compare the Markov model to a random baseline.

6.7.1 Transition Prediction and Accuracy

Each trial was represented as a sequence of visits to dispensers. Transition probabilities between dispensers were computed by tracking the frequency of transitions from one dispenser to another across all trials. The transition probability from dispenser i to dispenser j was defined following *Equation 3* (see Section 6.6.1.1).

After calculating these transition frequencies, each row of the transition matrix was normalized to ensure that the sum of outgoing transition probabilities from each dispenser was equal to 1. This normalization ensures that the transition matrix represents valid probability distributions for the Markov model, where each row is a probability distribution over the next possible dispensers.

6.7.1.1 Transition prediction Procedure

To evaluate the model's predictive capabilities, we compared the Markov model against a random baseline model. For the Markov model, the next dispenser choice was predicted based on the transition matrix computed from the data. Specifically, the prediction of the next dispenser for a given state i (current dispenser) is made by selecting the dispenser j with the highest transition probability:

Equation 7:

$$\hat{j} = \arg\max_{j} P\,(i \rightarrow j)$$

Where $\hat{j}$ is the predicted next dispenser and $P(i \rightarrow j)$ is the transition probability from dispenser i to dispenser j. As a baseline, a random model was implemented, where the next dispenser was selected uniformly at random from all dispensers. Prediction accuracy was calculated as the proportion of correct predictions, i.e., the proportion of times the predicted next dispenser matched the actual next dispenser.

6.7.1.2 Cross-Validation

To evaluate the robustness of the Markov model, we performed 10-fold cross-validation. The dataset was randomly split into 10 subsets (folds), with 9 folds used for training and the remaining fold used for testing. This process was repeated 10 times, with each fold serving as the test set once. For each fold, the transition matrix was computed based on the training data, and the prediction accuracy for both the Markov model and a random baseline model was evaluated on the test set. Performance metrics, including prediction accuracy, were then averaged across all folds to provide a reliable measure of the model's generalization capability.

In addition, confusion matrices were generated for each fold to analyze the predictions made by the Markov model. The final confusion matrix was obtained by averaging the confusion matrices across all folds, and each row was normalized so that the sum of probabilities for transitions from each actual dispenser equals 1. This normalization accounts for variations in transition frequencies and provides a clear picture of the model's performance on a per-dispenser basis.

Similarly, an error matrix was constructed by aggregating the counts of mispredicted dispensers across all folds. The error matrix was then normalized globally—by dividing each entry by the total number of errors across all folds—to yield a measure of the relative frequency of errors associated with each dispenser. The normalized error matrix highlights which dispensers are most prone to errors, offering insights into specific weaknesses in the model's predictions.

6.7.1.3 Evaluation and Statistical Comparison Between Models

To determine whether the Markov model significantly outperformed the random baseline in predicting individual transitions, we conducted a Wilcoxon signed-rank test on the accuracy scores obtained across the cross-validation folds. For both models, mean transition prediction accuracy was computed across folds to provide an overall performance measure. Variability was quantified by calculating the standard deviation and 95% confidence intervals (CI) of these accuracy scores. The Wilcoxon signed-rank test was then applied to assess whether the Markov model's transition accuracy was significantly higher than that of the random model, ensuring a robust statistical comparison.

6.7.1.4 Transition Matrix Visualization

To visualize the transition patterns learned by the Markov model, we generated predicted transition maps. These maps were represented as directed graphs, where nodes corresponded to dispensers and edges depicted the predicted transitions. The thickness of each edge was proportional to the corresponding transition probability, providing an intuitive visual representation of the local behavioral patterns captured by the model.

6.7.2 Sequence Prediction and Accuracy

To further evaluate the performance of the Markov model, we assessed its ability to predict full sequences of dispenser visits. Specifically, we focused on predicting sequences of 8 consecutive choices made by the marmoset. Instead of predicting transitions independently, we treated each sequence as a complete set of transitions to be predicted. Importantly, the same transition matrix computed from the training data in Section 6.7.1 was used for sequence predictions, ensuring consistency across both levels of analysis.

6.7.2.1 Sequence Prediction Procedure

For each sequence, predictions were generated using the same transition matrix from the training phase. The sequence was predicted iteratively, beginning with the first dispenser and selecting the next dispenser at each step based on the highest transition probability. Sequence prediction accuracy was then calculated as the proportion of correctly predicted sequences, representing the percentage of cases where the predicted sequence matched the actual sequence across all eight transitions. This approach assessed the Markov model's ability to capture global dependencies between transitions. To establish a baseline for comparison, a random model was also evaluated, where each dispenser was predicted with equal probability across all possible dispensers. The accuracy of the random model was computed using the same methodology, allowing for a direct performance comparison.

6.7.2.2 Cross-Validation for Sequence Prediction

To evaluate the generalization ability of the Markov model for sequence prediction, we applied 10-fold cross-validation, ensuring consistency with the methodology used in Section 6.7.1. The dataset was randomly divided into 10 folds, with each fold serving as a test set once while the remaining folds were used for training. For each fold, the transition matrix was computed from

the training sequences and used to predict sequences in the test set. Prediction accuracy was assessed for both the Markov and random models, allowing for a comparative evaluation of performance.

6.7.2.3 Evaluation and Statistical Comparison Between Models

To determine whether the Markov model significantly outperformed the random baseline in predicting sequences of dispenser visits, we conducted a Wilcoxon signed-rank test on sequence accuracy scores. Mean sequence accuracy across folds was computed for both models, providing an overall measure of prediction performance. Variability was quantified by calculating the standard deviation and 95% confidence intervals (CI) of these accuracy scores. The Wilcoxon signed-rank test was then applied to assess whether the Markov model's sequence accuracy was significantly higher than that of the random model, ensuring a robust statistical comparison.

6.7.2.4 Transition Matrix Visualization

To illustrate the predicted sequences, we constructed directed graphs in which nodes represent dispensers and edges represent the corresponding transition probabilities. In these graphs, only the sequence predicted by the Markov model was displayed. The thickness of each edge was scaled according to its transition probability, thereby highlighting the most likely transitions. This visualization provides an intuitive depiction of the predicted sequence and of how effectively the model captures global behavioral patterns.

6.7.3 Transition Prediction Accuracy Across Training Phases

To assess the evolution of the Markov model's performance over time, we evaluated its predictive accuracy separately for each training phase. This analysis allowed us to examine how the model adapted across different learning phases and whether prediction accuracy improved as training progressed.

6.7.3.1 Local Transition Prediction and Accuracy by Training Phase

The same Markov modeling approach described in Section 6.7.1 was applied independently to each training phase, with separate transition matrices computed for each phase. This ensured that any variations in transition dynamics across training could be captured. For each training phase, we calculated transition probabilities, predicted the next dispenser based on the highest transition probability, and compared the Markov model's accuracy to a random baseline.

6.7.3.2 Cross-Validation by Training Part

For cross-validation, the number of folds was dynamically adjusted based on the available data in each training phase. When sufficient sequences were available, 10-fold cross-validation was performed; otherwise, the number of folds was reduced accordingly to ensure reliable evaluation. Accuracy scores were averaged across folds to provide a robust measure of generalization within each training phase. Additionally, confusion matrices were computed separately for each training phase to analyze errors and evaluate model performance over time.

6.7.3.3 Evaluation and Statistical Comparison Between Models by Training Part

To determine whether the Markov model's performance improved throughout training, we compared accuracy across training phases as well as against the random baseline for each

phase. Variability was quantified by calculating the standard deviation and 95% confidence intervals (CI) of these accuracy scores. For each training phase, a Wilcoxon signed-rank test with Bonferroni correction was conducted to assess whether the Markov model significantly outperformed the random model. In addition, a Kruskal-Wallis test was performed to evaluate whether differences in accuracy across training phases were statistically significant. When the Kruskal-Wallis test indicated significant differences, Dunn's post-hoc test with Bonferroni correction was applied to identify which specific phases differed.

6.7.3.4 Transition Matrix Visualization by Training Part

To visualize how the Markov model's predictions evolved over training, we generated predicted transition maps for each training phase. These maps were represented as directed graphs, where nodes corresponded to dispensers and edges depicted the predicted transitions for that phase. The thickness of each edge was proportional to the corresponding transition probability, providing an intuitive visual representation of the transition patterns during each phase. This approach allowed us to track the evolution of local behavioral patterns as training progressed.

6.7.4 Sequence Prediction Accuracy Across Training Phases

Beyond individual transitions, we also evaluated the Markov model's ability to predict full sequences of dispenser visits separately for each training phase. This analysis allowed us to assess whether the model became more effective at capturing global behavioral patterns over time. Importantly, the same transition matrices computed from the training data for each training phase in Section 6.7.3 were used for sequence predictions, ensuring consistency across both levels of analysis.

6.7.4.1 Sequence Prediction and Cross-Validation by Training Part

For each training phase, sequences were extracted and analyzed separately, following the same Markov modeling approach as in Section 6.7.2. We used the transition matrices computed in Section 6.7.3 for each training phase. This ensured consistency across both transition- and sequence-level analyses.

Cross-validation was adapted dynamically to match the dataset size in each training part. 10-fold cross-validation was applied when enough sequences were available, while fewer folds were used when necessary to maintain a robust evaluation. In each fold, the precomputed transition matrix from the training phase was used to predict full sequences of up to 8 transitions in the test set. The Markov model's sequence accuracy was compared to that of a random baseline model, which predicted each transition with equal probability.

6.7.4.2 Evaluation and Statistical Comparison of Sequence Prediction

To assess whether the Markov model's sequence prediction accuracy significantly improved over training, a Wilcoxon signed-rank test with Bonferroni correction was conducted for each training phase to determine if the Markov model significantly outperformed the random baseline. Additionally, a Kruskal-Wallis test was applied to analyze whether sequence prediction accuracy evolved significantly across training parts. When the Kruskal-Wallis test indicated significant differences, Dunn's post-hoc test with Bonferroni correction was used to identify which specific training phases differed.

6.7.4.3 Sequence Transition Visualization

To illustrate the predicted sequences for each training phase, we constructed directed graphs in which nodes represent dispensers and edges represent the corresponding transition

probabilities. In these graphs, only the sequence predicted by the Markov model was displayed. The thickness of each edge was scaled according to its transition probability, thereby highlighting the most likely transitions for each training phase.

6.8. Analysis of Sequence Variability and Similarity

To further explore the structure of dispensers transition sequences, we analyzed the variability and similarity of observed sequences across error-free trials.

6.8.1 Identification of Unique Sequences and Frequency Analysis

Transition sequences were extracted from error-free trials, where each sequence was defined as a structured set of consecutive transitions between dispensers. The number of unique sequences was identified, and their relative usage frequencies were computed to evaluate the diversity of sequence patterns. To determine whether certain sequences were dominant behavioral patterns, we identified the most frequently used sequence for each animal and calculated its proportion relative to all observed sequences.

6.8.2 Analysis of Sequence Diversity

To quantify the diversity of navigation sequences used in error-free trials, we computed the normalized Shannon diversity index, which is derived from Shannon entropy and normalized by its theoretical maximum. The normalized Shannon index was defined as:

Equation 8:

$$H_{\text{norm}} = \frac{-\sum_{i=1}^{N} p_i \log_2 p_i}{\log_2 N}$$

where N is the total number of unique sequences, and p_i represents the relative frequency of sequence i, computed as the number of occurrences of that sequence divided by the total number of sequences.

This normalization ensures that H_{norm} ranges between 0 (when only one sequence is used, indicating no diversity) and 1 (when all sequences occur with equal probability, indicating maximum diversity).

6.8.3. Analysis of Sequence Similarity

To assess the structural similarity between sequences, we examined common transitions, defined as pairs of consecutive dispensers appearing within sequences. Sequence similarity was quantified using the Jaccard similarity index, calculated as:

Equation 9:

$$J(A, B) = \frac{|A \cap B|}{|A \cup B|}$$

Where A and B represent the sets of transitions in two sequences, and $|A \cap B|$ denotes the number of shared transitions between them. This index varies between 0 and 1, with 0 indicating no shared transitions and 1 indicating complete overlap. This measure provided insight into the degree of transition overlap, indicating whether sequences followed similar transition patterns or exhibited high variability.

We computed the mean Jaccard similarity across all sequence pairs and analyzed the distribution of similarity levels. Specifically, we determined the proportion of sequence pairs exceeding similarity thresholds ranging from 0.1 to 1.0, providing a detailed view of how frequently sequences shared a given percentage of their transitions. This approach allowed us to evaluate sequence overlap and assess the structural consistency of navigation patterns over trials.

To further examine sequence similarity patterns, the Jaccard similarity matrix was represented as a heatmap, where each cell indicated the similarity score between two sequences. This visualization provided a structured overview of sequence similarity distributions and facilitated the identification of clusters of highly similar sequences.

Additionally, to quantify the occurrence of individual transitions, we counted the frequency of each transition (i.e., movement from one dispenser to another) across all sequences. These frequencies were normalized by computing the percentage of sequences containing each transition relative to the total number of sequences analyzed.

6.8.4 Sequence Diversity Across Training Phase

To examine the evolution of sequence diversity over training, we computed the normalized Shannon diversity index separately for each training phase (as described in Section 6.8.2). To model the trajectory of diversity across training, we applied weighted least squares (WLS) quadratic regression, with weights determined by the number of trials in each phase to account for sample size differences. We compared the performance of a simple linear regression to that of the quadratic model to determine whether a non-linear (e.g., U-shaped) trend provided a better fit. Model fit was evaluated using R^2 values, and the statistical significance of the quadratic term was examined. Prior to interpreting the results, we verified that the model assumptions—normality of residuals, homoscedasticity, independence of errors, and absence of multicollinearity—were met, confirming the reliability of our approach.

6.8.5 Dominant Sequence Frequency, New Sequence Ratio, and Reused Sequence Ratio Across Training Phases

To examine how sequence selection evolved throughout training, we quantified three key metrics: dominant sequence frequency, new sequence ratio, and reused sequence ratio. These measures were computed separately for each training phase to assess changes in the patterns of sequence selection over time.

6.8.5.1 Dominant Sequence Frequency

The dominant sequence was identified as the most frequently occurring sequence across all error-free trials. For each training part, we computed its frequency of use, defined as the proportion of trials in which the dominant sequence was executed.

6.8.5.2 New Sequence Ratio

The new sequence ratio was computed as the number of unique sequences in each training phase that had not been observed in any previous phase. This metric was calculated iteratively

by maintaining a cumulative set of previously encountered unique sequences and identifying, for each phase, the fraction of new unique sequences relative to all unique sequences observed during that phase

6.8.5.3 Reused Sequence Ratio

The reused sequence ratio was computed as the proportion of sequences in each training phase that had already been observed in previous phases. For each training phase, reused sequences were identified by comparing the sequences in the current phase to a cumulative set of sequences encountered in earlier phases. The reused sequence ratio was then calculated as the total number of reused sequences divided by the total number of sequences in that phase.

6.8.5.4 Correlations Between Sequence Diversity and Sequence Selection Metrics

To assess the relationship between sequence diversity and sequence selection patterns, we computed Pearson correlations between the normalized Shannon diversity index and each of the three metrics (dominant sequence frequency, new sequence ratio, and reused sequence ratio). Pearson's correlation coefficients and corresponding p-values were used to quantify the strength and significance of these relationships. Additionally, linear regression lines were included in the correlation plots to visualize potential trends.

6.8.6 Sequence Similarity Across Training Phases

To assess how sequence similarity evolved throughout training, we applied the same Jaccard similarity analysis described in Section 6.8.3, computed separately for each training phase. For each phase, sequences were extracted and the pairwise Jaccard similarity index was calculated to quantify the overlap in transitions between sequences. Mean similarity scores and SEM were computed to evaluate whether sequences became more homogeneous or remained diverse over time. Additionally, a Jaccard similarity matrix was generated for each training phase and visualized as a heatmap, illustrating the structural similarity across trials. To determine whether sequence similarity significantly varied across training phases, we performed a Kruskal-Wallis test on the similarity scores; when significant differences were observed, Dunn's post-hoc test with Bonferroni correction was applied to identify specific pairwise differences.